Evaluation of Sentinel-1 and Sentinel-2 Feature Sets for Delineating Agricultural Fields in Heterogeneous Landscapes

GIDEON OKPOTI TETTEH[1], **ALEXANDER GOCHT**[1], **STEFAN ERASMI**[1], **MARCEL SCHWIEDER**[1,2], **AND CHRISTOPHER CONRAD**[3]

[1]Thünen Institute of Farm Economics, 38116 Braunschweig, Germany
[2]Geography Department, Humboldt University of Berlin, 10099 Berlin, Germany
[3]Institute of Geosciences and Geography, Martin-Luther-University Halle-Wittenberg, 06099 Halle, Germany

Corresponding author: Gideon Okpoti Tetteh (gideon.tetteh@thuenen.de)

ABSTRACT The Group on Earth Observations Global Agricultural Monitoring Initiative (GEOGLAM) considers agricultural fields as one of the essential variables that can be derived from satellite data. We evaluated the accuracy at which agricultural fields can be delineated from Sentinel-1 (S1) and Sentinel-2 (S2) images in different agricultural landscapes throughout the growing season. We used supervised segmentation based on the multiresolution segmentation (MRS) algorithm to first identify the optimal feature set from S1 and S2 images for field delineation. Based on this optimal feature set, we analyzed the segmentation accuracy of the fields delineated with increasing data availability between March and October of 2018. From the S1 feature sets, the combination of the two polarizations and two radar indices attained the best segmentation results. For S2, the best results were achieved using a combination of all bands (coastal aerosol, water vapor, and cirrus bands were excluded) and six spectral indices. Combining the radar and spectral indices further improved the results. Compared to the single-period dataset in March, using the dataset covering the whole season led to a significant increase in the segmentation accuracy. For very small fields (< 0.5 ha), the segmentation accuracy obtained was 27.02%, for small fields ($0.5 - 1.5$ ha), the accuracy was 57.65%, for medium fields (1.5 ha $- 15$ ha), the accuracy was 75.71%, and for large fields (> 15 ha), the accuracy stood at 68.31%. As a use case, the segmentation result was used to aggregate and improve a pixel-based crop type map in Lower Saxony, Germany.

INDEX TERMS Agricultural field delineation, band indices, essential agricultural variables, feature combination, image segmentation, intersection over union, remote sensing, segmentation optimization.

I. INTRODUCTION

As part of its activities geared towards ensuring the attainment of the United Nation's Sustainable Development Goals [1], the Group on Earth Observations Global Agricultural Monitoring Initiative (GEOGLAM[1]) identifies agricultural fields as one of its essential agricultural variables [2]. Additionally, agricultural fields are valuable inputs to subsequent processes such as crop type mapping [3], analysis of crop rotations [4], implementation of crop management activities [5], and the control of subsidy payments to farmers [6]. Conventionally, agricultural fields have been

The associate editor coordinating the review of this manuscript and approving it for publication was John Xun Yang.

[1]https://earthobservations.org/geoglam.php (Accessed: Jul. 9, 2021).

generated through the manual digitization of hardcopy maps (aerial images, topographic maps, etc.) [7] or direct field measurements. The obvious problem with those approaches is that they are costly and inefficient especially as agricultural maps require continuous updates to capture the real-time or near real-time events happening on agricultural fields. The use of remote sensing (RS) is a good alternative for mapping agricultural fields given that satellite images can be acquired over wide geographical areas at a high temporal resolution [8]–[10].

The use of satellite images to delineate agricultural fields has an extensive history in the RS world. It can largely be attributed to the use of medium spatial resolution satellites like Landsat. For example, to extract agricultural fields, numerous studies [7], [11]–[14] used the Landsat

Thematic Mapper (TM), some [13]–[16] employed the Landsat Enhanced Thematic Mapper Plus (ETM+), and others [17]–[20] used the Landsat 8 Operational Land Imager (OLI). The common theme running through all of those studies is the use of image segmentation as a means of extracting the boundaries of the agricultural fields.

Image segmentation, which is the process of partitioning an image into homogeneous and distinct objects, is the foundation of the object-based image analysis (OBIA) paradigm [21]. The growth of the OBIA paradigm was fueled by the advent of high-resolution images and the availability of powerful computing environments [22]. It was observed in [23] that the spatial resolution of an image has a direct impact on the outcome of image segmentation. In [5], the authors established that the higher the spatial resolution, the higher the coverage of agricultural fields eligible for site-specific services like the monitoring of the Common Agricultural Policy (CAP) [24] and the application of smart farming technologies. Therefore, high or very high spatial resolution images are generally preferred for segmenting agricultural fields. For example, pan-sharpened SPOT-5 images were used by [4], RapidEye by [25], WorldView-2/3 by [26], QuickBird by [27], and digital orthophotos by [6]. However, for mapping large geographical areas, the use of high or very high spatial resolution images becomes infeasible as they become extremely expensive to acquire. Therefore, medium spatial resolution images remain the most viable option for delineating agricultural fields at regional, national, and global scales at little to no cost.

Although Landsat images have proven useful for mapping agricultural fields over large areas, the spatial resolution of 30 m is often unable to resolve individual agricultural fields thereby inhibiting field-based applications in many cropping systems around the world [28]. Building on the experiences of the Landsat and SPOT missions, Sentinel-2 (S2) was designed within the framework of the European Copernicus program for land surface and agriculture monitoring [28] at a temporal resolution of 5 days and a spatial resolution of 10 m. As opposed to optical sensors, which are inhibited by clouds, Sentinel-1 (S1), which is also part of the Copernicus program enables the continuous monitoring of the earth's surface in all weather conditions at a temporal resolution of 6 days and a spatial resolution of 20 m. Various researchers have used S1 [29], [30], and predominantly S2 [31]–[40] for segmenting agricultural fields. In using the S1 or S2 images, most of those authors used existing segmentation algorithms (e.g., [29], [30], [32]–[34], [36]–[40]), some proposed new segmentation algorithms (e.g., [31], [35]), and others proposed new segmentation parameter optimization approaches (e.g., [36], [37]). One area that is yet to be comprehensively explored is the determination of the optimal feature set from S1 and S2 images for segmenting agricultural fields given that both sensors come with different bands and additional features like band indices can be calculated as well. In an experiment based on a WorldView-2 image, the authors of [23] showed that the feature set used as the input to the segmentation algorithm has an impact on the segmentation result. Therefore, it is worth exploring different S1 and S2 feature sets to assess their impact on the segmentation of agricultural fields.

Beyond the feature set, agricultural fields are dynamic and change throughout the growing season, thereby requiring continuous updates. Therefore, it is also relevant to analyze the accuracy at which the agricultural fields can be delineated from the S1 and S2 feature datasets at different times of the growing season. Further, it is important to assess the accuracy at which agricultural fields can be segmented from S1 and S2 at different agricultural landscapes with different field sizes. In [2], the authors categorized three different field sizes: small fields (< 1.5 ha), medium fields (1.5 ha $- 15$ ha), and large fields (> 15 ha). They subsequently asserted that medium spatial resolution images (here S1 and S2) are more suitable for delineating large fields. Based on their respective spatial resolutions, S1 and S2 should be capable of spatially resolving small fields. For example, a 1 ha field should be spatially resolved by S1 using 25 pixels and S2 using 100 pixels. Therefore, the validity of the assertion in [2] ought to be tested. Further, it remains to be seen what segmentation accuracy can be achieved for those three field size categories.

To fill all the aforementioned gaps, we set out in this study to execute the following objectives: (1) identify the optimal feature set from S1 and S2 images for segmenting agricultural fields, (2) analyze the evolution of the accuracy of agricultural fields segmented from the S1 and S2 feature sets throughout the growing season, and (3) assess the accuracy that can be achieved for different field sizes. To achieve our objectives, we employed the multiresolution segmentation (MRS) algorithm [41] in eCognition [42] to segment agricultural fields from different feature sets generated from S1 and S2 images acquired between March and October of 2018 in Lower Saxony, Germany.

II. STUDY AREA & DATA
A. STUDY AREA
The federal state of Lower Saxony in Germany was selected as the study area (Figure 1). Its total area of about 4,770,041 ha has a mostly flat terrain and is located in the temperate climate zone of Europe [36]. The majority of its landmass is covered by agricultural lands that are mostly dominated by grasslands, summer cereals, winter cereals, potatoes, winter rapeseed, and sugar beet [36]. For efficient segmentation purposes, the study area was divided into 575 tiles. Each tile is 10 km by 10 km.

To enable the smooth merger of the segmentation results from all the tiles, the geometry extent of each tile was extended or shrunk to cover the geometry of all polygons contained in the agricultural land-cover (LC) dataset (see Section II.C for the description of the dataset) whose centroids intersected that particular tile. Consequently, the extended or shrunk tiles (symbolized as blue outlines in Figure 1) have variable sizes with the average size being 11 km by 11 km. To reduce the computation time
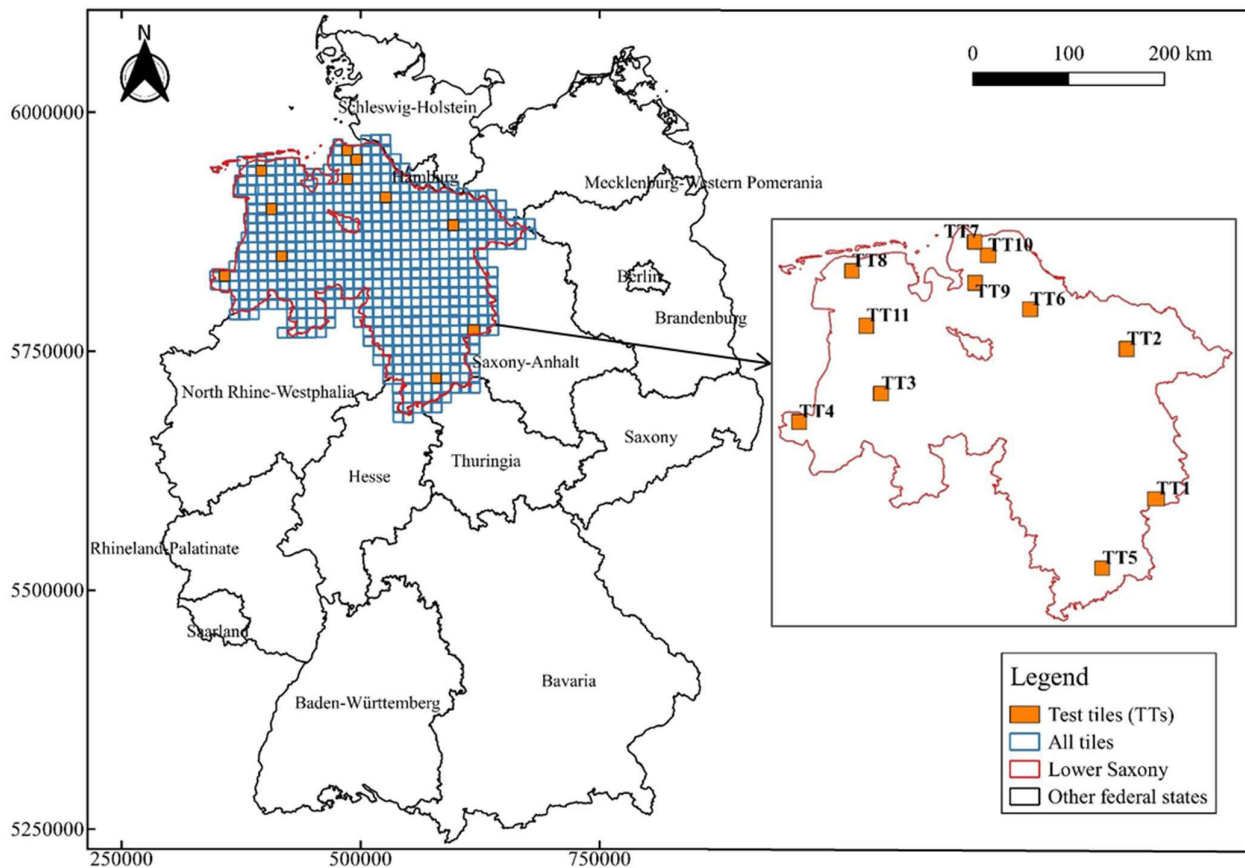
FIGURE 1. The study area (Lower Saxony) used in this study. A total of 575 tiles (blue outline) were created over Lower Saxony. The test tiles (TTs) used as the basis to identify the optimal feature sets are symbolized in orange color. All the coordinates in the figure are in UTM Zone 32N (EPSG:32632).

needed to identify the optimal feature set, we manually assessed and selected eleven test tiles (TTs) (symbolized as orange polygons in Figure 1) whose landscape compositions were representative of the remaining tiles in Lower Saxony. Details on how the selection was done are treated in Section III.A.

B. SATELLITE DATA
A recent study [43] demonstrated the usability of monthly composites of S1 and S2 images for large-scale mapping of agricultural land-use (LU) types. For our study, we used monthly mean composites (MMCs) of S1 and S2 images from March to October 2018. For the MMCs of S1, we downloaded the Sentinel-1 L3 BS (Sentinel-1 Level-3 Backscatter) data from CODE-DE (Copernicus Data and Exploitation Platform – Deutschland).[2] CODE-DE is a cloud computing platform that provides access to the datasets of the Copernicus program covering Germany as well as virtual machines for data processing. The Sentinel-1 L3 BS images in VV and VH polarizations are created by averaging all the Sentinel-1 L2 CARD-BS (Sentinel-1 Level-2 Copernicus Analysis Ready Data – Backscatter) images over a month. The Sentinel-1 L2

CARD-BS images, which come at a resampled spatial resolution of 10 m, are generated by processing the Level-1 (L1) Ground Range Detected (GRD) images of S1 acquired in the Interferometric Wide Swath (IW) mode. The processing is done by CODE-DE with the Sentinel Application Platform (SNAP) using the standard procedure of applying an orbit file, removing GRD border noise, removing thermal noise, calibration, and terrain correction [44].

For S2, we used FORCE (Framework for Operational Radiometric Correction for Environmental monitoring) [45]. FORCE is a processing software for generating higher-level analysis-ready data (ARD) from S2 and Landsat images. Based on the top-of-atmosphere L1C images of S2, FORCE generates bottom-of-atmosphere L2 ARD images by correcting for atmospheric, geometric, and bidirectional reflectance distribution function (BRDF) effects [46]–[48]. In FORCE, clouds and cloud shadows are detected and masked using the Fmask algorithm [49]–[51]. The cloud and cloud shadow pixels were replaced using an interpolation method based on an ensemble of radial basis function (RBF) convolution filters [52]. FORCE outputs all S2 bands except the ones with a spatial resolution of 60 m, i.e., the coastal aerosol, water vapor, and cirrus bands. The bands with a spatial resolution of 20 meters are resampled to 10 m. For each band, all pixel

---

[2] https://code-de.org/en/ (Accessed: Jul. 9, 2021).

values belonging to the same month were averaged to obtain the MMCs for S2.

C. AGRICULTURAL LAND-COVER

From the digital landscape model of the German Official Topographic Cartographic Information System (ATKIS) of 2018, we extracted the vector layer containing polygons of the agricultural LC (arable land and grassland) present at the tiles. This layer was used to create a mask to remove non-agricultural areas from the MMC images before segmenting the agricultural fields. This approach has also been used in other studies [31], [36], [37].

D. REFERENCE DATA

For segmentation evaluation and optimization, we used the Geospatial Aid Application (GSAA) data of 2018 covering the TTs. This data was obtained from the Lower Saxony Ministry of Food, Agriculture, and Consumer Protection. The GSAA data contains the boundaries of agricultural parcels manually digitized from very high-resolution orthoimages (spatial resolution ≤ 1 m) by farmers intending to access the subsidies within the CAP framework. The LU type (e.g., mowing pasture, meadow, maize, winter wheat, etc.) of each agricultural parcel is additionally declared by the farmer. The average size of an agricultural parcel over the TTs is about 3.4 ha, with the minimum size being about 0.2 ha and the maximum size being about 63 ha. The average number of agricultural parcels per tile is 2,463. For each test tile, basic descriptive information of the GSAA parcels can be found in Table 5 of Appendix A.

III. METHODOLOGY

The workflow we used in this study is depicted in Figure 2. The components of the workflow will be explained in the next subsections.

A. SELECTION OF TEST TILES (TTs)

The selection of the TTs was based on four criteria namely a high percentage coverage of agricultural LU, a high number of reference parcels for segmentation evaluation, the presence of both big and small agricultural fields, and a variable shape factor (SF) distribution per tile. The selected TTs are more dominated by agricultural LU as depicted in Figure 14 (Appendix A). Each selected tile contains a mixture of both big and small fields (see Table 5 of Appendix A). The authors in [36] and [53] emphasized the importance of having a sizeable number of reference objects for supervised segmentation evaluation to ensure accurate results. In our study, the minimum number of reference fields was 1,622 at TT2, which we considered as a sizeable number. The SF was used to quantify the shape characteristics of the GSAA parcels within each tile. We adopted the SF method in (1) as was proposed by [54];

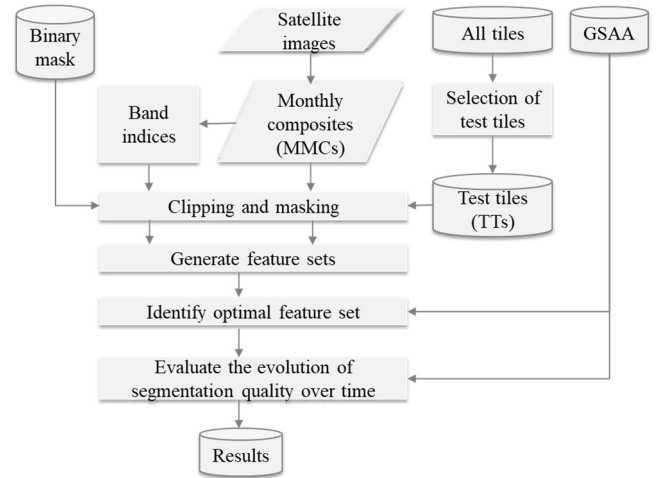$$SF = \frac{4 * \Pi * Area\,(X)}{(Perimeter\,(X))^2} \qquad (1)$$

FIGURE 2. The workflow we followed in this study.

where X is a GSAA parcel. For each tile, the SF factor is calculated for all GSAA polygons. Higher SF values indicate more compact polygons, while lower values represent more elongated or irregular-shaped polygons. The selected tiles have variable SF distributions as captured by Figure 15 (Appendix A).

B. BAND INDICES

Eight band indices (two radar and six optical) (Table 1) with extensive usage in RS for mapping agricultural lands were used in this study. The radar and optical indices were computed using the MMC images of S1 and S2, respectively. All the indices required at least two bands for computation. Given that the S2 MMC images had ten bands, the optical indices were selected to cover different parts of the electromagnetic spectrum as was previously done in [3]. The S1 MMC images come with only two bands, hence each radar index used both bands for computation.

C. CLIPPING AND MASKING

Each MMC and band index of S1 and S2 was clipped to the boundary of a test tile. After clipping, all non-agricultural areas were removed. The agricultural vector layer extracted from ATKIS was used for this purpose. This vector layer contains cadastral polygons of all agricultural lands in Germany. We applied a negative buffer distance of 5 m to each polygon to create a separation between two adjacent polygons that share a common boundary. The reason for the negative buffer was to ensure the ease of separation between adjacent agricultural fields in the images during the segmentation process. All pixels outside the buffered polygons were masked out from each MMC and band index. These masked images were used for all subsequent processes.

D. GENERATE FEATURE SETS

A feature set is a combination of two or more features (bands, indices). In all, nine feature sets were created (Table 2). The table shows each feature set alongside the input features that

TABLE 1. The utilized radar and optical indices, abbreviations, formulas, and sources in the literature.

Satellite	Index	Formula	Source
S1	Cross Ratio (CR)	$\dfrac{VH}{VV}$	[55]
	Radar Vegetation Index (RVI)	$\dfrac{4 * VH}{VV + VH}$	[56]
S2	Green Vegetation Index (GVI)	$\dfrac{Green - Red}{Green + Red}$	[57]
	Normalized Difference Vegetation Index (NDVI)	$\dfrac{NIR - Red}{NIR + Red}$	[58]
	Normalized Differential Senescent Vegetation Index (NDSVI)	$\dfrac{SWIR1 - Red}{SWIR1 + Red}$	[59]
	Normalized Difference Red Edge Index (NDRE)	$\dfrac{NIR - RedEdge1}{NIR + RedEdge1}$	[60]
	Normalized Difference Water Index (NDWI)	$\dfrac{NIR - SWIR1}{NIR + SWIR1}$	[61]
	Normalized Difference Tillage Index (NDTI)	$\dfrac{SWIR1 - SWIR2}{SWIR1 + SWIR2}$	[62]

TABLE 2. The nine feature sets used for optimization: data sources, names, and lists of input features.

Satellite	Feature set	Input features
S1	S1B	VH, VV
	S1I	CR, RVI
	S1BI	S1B, S1I
S2	S2B4	Blue, Green, Red, NIR
	S2B10	Blue, Green, Red, RedEdge 1, RedEdge 2, RedEdge 3, NIR, Narrow NIR, SWIR1, SWIR2
	S2I	GVI, NDVI, NDSVI, NDRE, NDWI, NDTI
	S2B4I	S2B4, S2I
	S2B10I	S2B10, S2I
S1 & S2	S2S1I	S2I, S1I

were used to create it. Three feature sets were based on S1 and five were based on S2. Those S1 and S2 feature sets were created after conducting some pretests to assess the separate impact of the bands and band indices on the segmentation accuracy. During the conduction of the pretests, we realized that a combination of the radar and optical indices led to an increase in the segmentation accuracy, hence the creation of the combined feature set named S2S1I. Based on each feature set, a feature dataset was generated for each month in the growing season using the masked images created in section III.C.

E. IDENTIFY OPTIMAL FEATURE SET
For each feature set in Table 2, all feature datasets from March to October were stacked together to create a seasonal

feature dataset. Nine seasonal feature datasets were created per tile. To optimize the segmentation of those nine seasonal feature datasets per tile, we used the supervised segmentation optimization (SSO) approach of [36]. That SSO approach utilizes the MRS algorithm. Given that the MRS algorithm requires three main parameters (scale, shape, and compactness), all of which take a varied range of input values, that SSO approach uses Bayesian optimization to identify the single parameter combination that yields the optimal segmentation output. The accuracy of the segmentation output of each parameter combination is measured through the overall segmentation quality (OSQ) metric, which is an area-weighted average of the Jaccard index [63]. The Jaccard index, which is widely known as Intersection over Union (IoU), is frequently used in computer vision tasks to measure the geometric similarity between a reference object and a target object extracted from an image or a video. The formula for IoU and OSQ as culled from [36] is given in (2) and (3), respectively;

$$IoU(Y) = \frac{Area\,(X \cap Y)}{Area\,(X \cup Y)} \tag{2}$$

$$OSQ = \frac{\sum_{i=1}^{n} Area(Y_i) * IoU(Y_i)}{\sum_{i=1}^{n} Area(Y_i)} \tag{3}$$

where X is a reference object, Y is its target object (segment), $X \cap Y$ is the spatial intersection between them, $X \cup Y$ represents their spatial union, and n is the total number of segments in a segmentation output. Given an input image and a reference dataset (GSAA in our case), the SSO approach uses 150 parameter combinations and then returns the segmentation output that best matches the reference data. It also returns the corresponding OSQ value as well as the IoU value of each segment in the optimal segmentation output. Both IoU and OSQ range from zero (lowest segmentation quality) to one (highest segmentation quality). The feature set with the highest average OSQ over the eleven tiles was adjudged as the best.

F. EVALUATE THE EVOLUTION OF SEGMENTATION ACCURACY OVER TIME
To assess the evolution of the segmentation accuracy of agricultural fields over time, we created incremental feature datasets covering different months of the growing season based on the optimal feature set identified in section III.E. Table 3 shows how the incremental feature datasets were created. The first incremental feature dataset (DID-1) was created using the feature dataset of March only. The one in April (DID-2) contains the feature datasets of March and April. This incremental process continued up to October (DID-8). DID-8 is the same as a seasonal feature dataset described in section III.E. The number of bands in each incremental feature dataset varied. Assuming S2B4 was established as the optimal feature set, DID-1 will have four bands, DID-2 will contain eight bands, and DID-8 will have 32 bands. For each of the eleven tiles, eight incremental feature datasets were created. Each incremental feature dataset

TABLE 3. The incremental feature datasets (DID-1 to DID-8) that were created in this study. The "x" symbol means that the feature dataset of that month was used in creating the incremental feature dataset.

Dataset ID	Mar	Apr	May	Jun	Jul	Aug	Sep	Oct
DID-1	x							
DID-2	x	x						
DID-3	x	x	x					
DID-4	x	x	x	x				
DID-5	x	x	x	x	x			
DID-6	x	x	x	x	x	x		
DID-7	x	x	x	x	x	x	x	
DID-8	x	x	x	x	x	x	x	x

served as an input to the SSO approach and the corresponding results were recorded.

IV. RESULTS

A. OPTIMAL FEATURE SET FOR SEGMENTATION

Figure 3 shows the variability of OSQs obtained at the eleven TTs for each feature set as well as the average OSQ (cyan boxes) obtained by each feature set over the test tiles. The S1 feature set based on only the radar indices (S1I) outperformed the one based on only the radar bands (S1B). The combination of the radar bands and indices (S1BI) led to an increase in OSQ. The feature set purely based on the S2 indices (S2I) outperformed those purely based on the spectral bands (S2B4, S2B10). The combination of the S2 bands and S2I to respectively create S2B4I and S2B10I improved the segmentation results as compared to separately using either S2B4 or S2B10. Among the feature sets based on only the S2 bands, S2B4 yielded better results than S2B10. The combination of the S2 and S1 indices (S2S1I) obtained the highest average OSQ. The numerical values of the average OSQs obtained by the feature sets over all the test tiles are reported in Table 6 of Appendix A.

The breakdown of the performance of each feature set per tile is shown in Figure 4. S2S1I yielded the best results at three tiles (TT3, TT4, TT10), S2B10I at three tiles (TT2, TT8, TT11), S1BI at two tiles (TT1, TT5), S1I at two tiles (TT6, TT7), and then S2B4I at one tile (TT9).

The optimal parameter combinations associated with S1BI (optimal among the S1 feature sets), S2B10I (optimal among the S2 feature sets), and S2S1I (overall optimal feature set) per tile are shown in Table 7 of Appendix A.

To understand the differences in OSQ between the feature sets, we further investigated S1BI, S2B10I, and S2S1I. We generated the area-weighted histogram in Figure 5 with ten bins using the IoU computed for each segment in the optimal segmentation results that were respectively obtained by S1BI, S2B10I, and S2S1I at all test tiles. We created an area-weighted histogram because the OSQ is also area-weighted. To create the histogram, each IoU contributed its segment area to the bin count (frequency) instead of one. As the histogram shows, the S2S1I feature set generated more

segments with better geometric matches to the GSAA parcels than the other feature sets, which resulted in it obtaining the highest average OSQ. Compared with S2B10I and S2S1I, the higher values for low-IoU bins obtained by S1BI as shown in Figure 5 explain its low accuracies in Figure 3 and Figure 4.

Based on the best feature set (S2S1I), we visually inspected the optimal segmentation results at TT1 (highest OSQ of 73.7%) and TT10 (lowest OSQ of 59.9%) to understand the reasons behind the difference in OSQ between them. Figure 6 shows the segmentation results achieved at TT1 and TT10. The false-color image of S2S1I at TT1 and TT10 are depicted in Figure 6a and Figure 6b, respectively. The GSAA parcels (black outlines) have been overlaid on the false-color images in Figure 6c and Figure 6d, respectively. The optimal segments symbolized by their respective IoU values have been overlaid on the false-color images in Figure 6e and Figure 6f, respectively. The segments that touch the boundaries of each tile are excluded in the SSO approach because they are artifacts, hence they are not displayed in Figure 6e and Figure 6f. The reason for the difference in OSQ between those two tiles is attributable to the difference in the size and shape of agricultural fields at each tile. At TT1, the tiles are bigger and more compact. The opposite can be seen at TT10, where most of the agricultural fields are smaller and less compact (more elongated).

B. EVOLUTION OF SEGMENTATION ACCURACY OVER TIME

The average OSQ attained by each S2S1I-based incremental feature dataset over all tiles is depicted in Figure 7. The lowest OSQs were mostly obtained at the beginning of the growing season in March with DID-1. As the season progressed and more datasets were acquired and used, the segmentation accuracy increased accordingly. The highest OSQs were mostly achieved at the end of the growing season in October (DID-8). As Figure 8 shows, the optimal OSQ at eight tiles (TT1, TT4, TT5, TT6, TT7, TT8, TT9, TT11) was attained with DID-8, two tiles (TT2, TT3) with DID-7, and one tile (TT10) with DID-4. The difference in average OSQ of 5.31 percentage points between DID-1 (62.2%) and DID-8 (67.51%) was observed to be statistically significant (p-value = 0.006) based on a two-tailed t-test. In the incremental segmentation set-up, the highest improvement in OSQ of almost 2% was achieved by adding the May dataset to the incremental stack to create DID-3. This was followed by the addition of the June dataset to create DID-4, which led to an increase of about 1.2%. After June, the increase became more gradual.

We used the IoU values of the segments in the optimal segmentation results generated with the incremental feature datasets to create the area-weighted histogram shown in Figure 9, which focuses on DID-1 (start of the season), DID-3 (after the farmers submit their GSAA), and DID-8 (end of the season). The optimal segmentation results respectively obtained with DID-3 and DID-8 produced more segments that geometrically matched the GSAA parcels than DID-1 did.
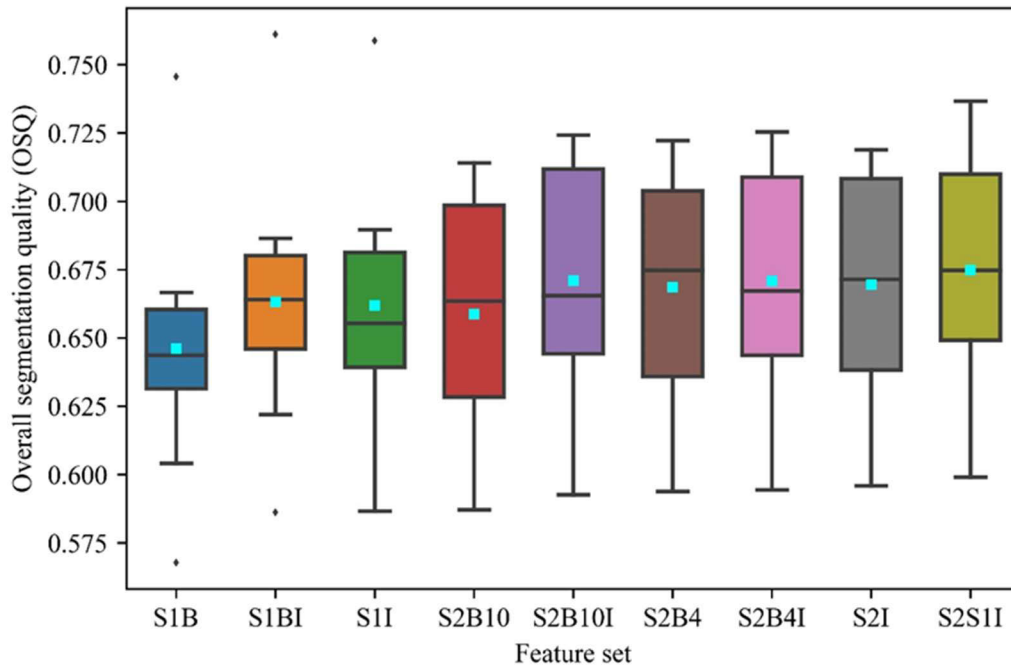
FIGURE 3. Boxplots showing the variability of OSQs obtained at the eleven tiles per feature set. The cyan boxes represent the average OSQs achieved by each feature set over the tiles. The within-box horizontal lines are the median OSQs. The black dots are the OSQs that are outliers.
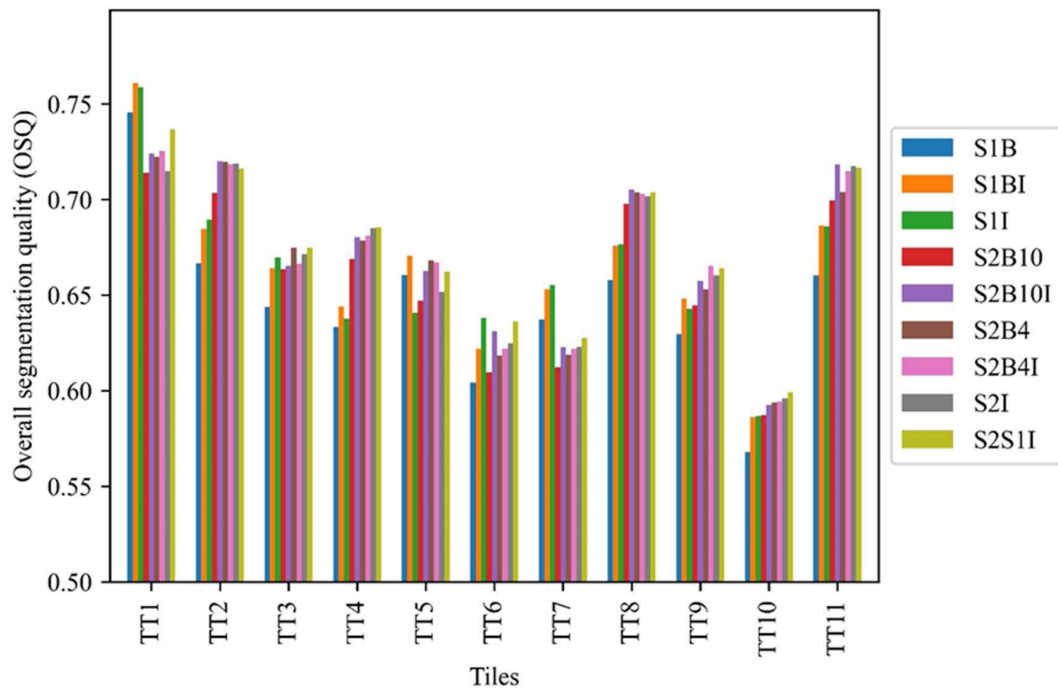

FIGURE 4. The OSQ obtained by each feature set per tile.

C. PLAUSIBILITY ANALYSIS: COMPARISON OF THE SEGMENTATION RESULTS WITH THE GSAA PARCELS

In [36], over-segmentation was identified as the main reason for the disparity between the GSAA parcels and the segmentation results. In addition to the instances of over-segmentation established in [36], we identified a new instance of over-segmentation, which was caused by the masking approach we used in this study as shown in Figure 10.

In Figure 10a, the GSAA parcel indicates the presence of a single LU (mowing pasture) but due to the inward buffer applied at the masking stage, an artificial boundary was created in the satellite image leading to the incorrect generation of two separate segments (B1, B2) as shown in Figure 10b. B1 and B2 had moderate IoU values of 51% and 35.9%, respectively. A higher IoU value could have been achieved with a single segment without any separation between them.
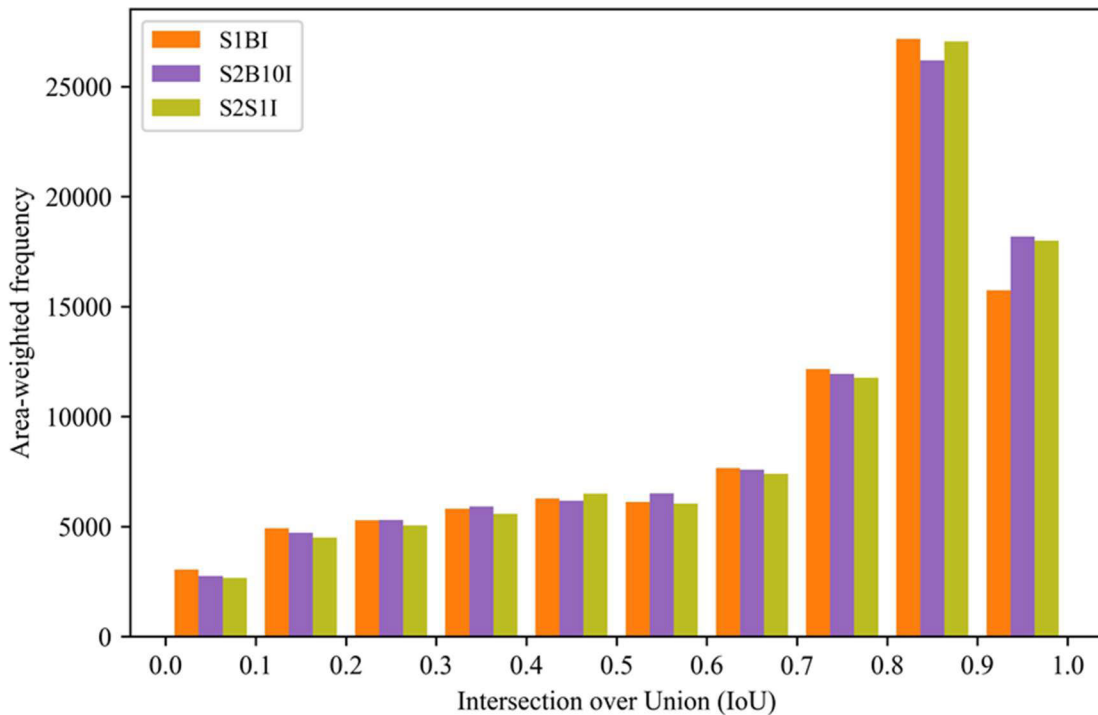
FIGURE 5. Area-weighted histogram of the Intersection over Union (IoU) values computed for the segments in the optimal segmentation results achieved respectively by S1BI, S2B10I, and S2S1I at all test tiles.

TABLE 4. Overall segmentation quality (OSQ) computed for the different field size categories.

Field size group	OSQ
Very small (< 0.5 ha)	27.03%
Small (0.5 − 1.5 ha)	57.65%
Medium (1.5 − 15 ha)	75.71%
Large (> 15 ha)	68.31%

D. SEGMENTATION ACCURACY FOR DIFFERENT FIELD SIZES

The segmentation optimization process was subsequently extended to the other tiles in Lower Saxony based on the DID-8 generated for S2S1I. The optimal segmentation results of the 575 tiles were then merged. The merged result can be viewed as the "original_segmentation_ni" layer on this web map.[3] Based on this merged result, we analyzed the impact of the area of the agricultural fields on the OSQ. In [5], the authors stated that a minimum of 50 pixels per field is the critical number required for site-specific smart farming. Therefore, we separated the small field size category of [2] into two sub-groups: very small fields (< 0.5 ha) and small fields (0.5 ha – 1.5 ha). The medium and large field categories were kept. Table 4 shows the OSQ computed for each category.

From Table 4, the accuracy of large fields was lower than the medium fields. A visual assessment of the results revealed some of the instances that contributed to that phenomenon as shown in Figure 11 and Figure 12, where the size of the GSAA parcels are 19.6 ha and 15.7 ha, respectively. To receive the greening payments within CAP, farmers with arable land exceeding 15 ha have to use at least 5% of their land as an Ecological Focus Area (EFA), e.g., hedges. Due to the presence of hedges in Figure 11a, the SSO correctly created one segment containing the hedges (B1) and a second segment without hedges (B2) as captured in Figure 11b. Unfortunately, B1 had a low accuracy of 6.4%. B2 was 86.4% accurate. In Figure 12, although the image (Figure 12a) looks relatively homogenous, two separate segments (B1 and B2) with respective accuracies of 21.3% and 73.9 % were created by the SSO as shown in Figure 12b. This is an error caused by the MRS parameters not being optimal for that particular agricultural field, even though the identified parameters were optimal for the tile that contains that field.

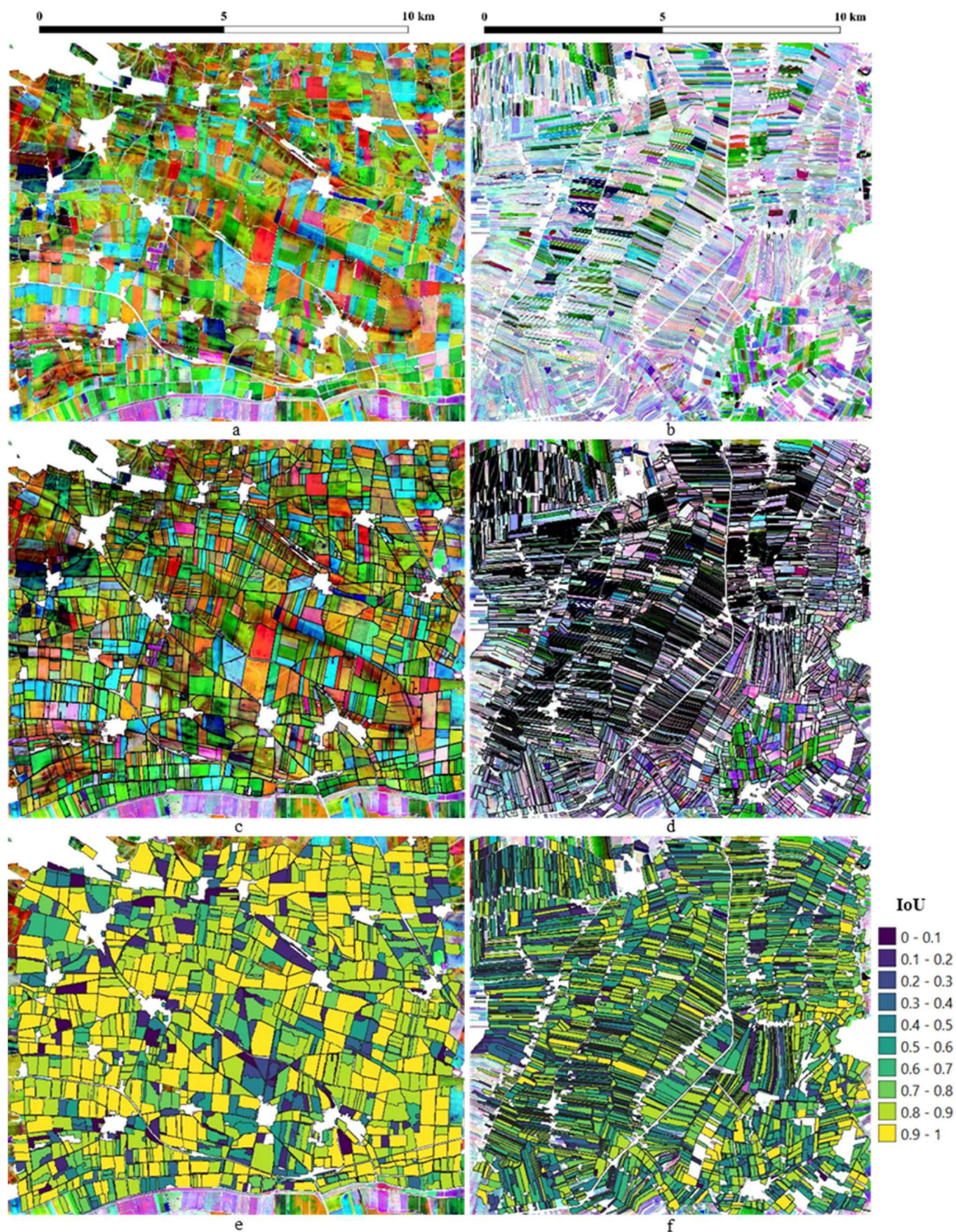## E. USE CASE: POST-FILTERING OF PIXEL-BASED CROP MAPS

In [64], the authors showed that the post-filtering of pixel-based crop type maps using image segments through majority voting can improve image classification results. Therefore, as a use case, we tested if the crop type map of [65] as visualized on this webpage[4] could be improved using the merged segmentation result of Lower Saxony. Before proceeding with this test, we first post-processed the merged segments in GRASS GIS.[5] We applied "v.clean" to first

---

[3]https://tisdex.thuenen.de/maps/34/view#/ (Accessed: Jul. 9, 2021).

[4]https://ows.geo.hu-berlin.de/webviewer/croptypes/ (Accessed: Jul. 9, 2021).

[5]https://grass.osgeo.org/ (Accessed: Jul. 9, 2021).

FIGURE 6. Optimal segmentation results obtained at TT1 (left column) and TT10 (right column) based on S2S1I. (a) and (b) show the false-color composites of the NDVI MMCs of March, June, and October. The GSAA parcels (black outlines) have been overlaid on the respective images at (c) and (d). The optimal segments have been symbolized with their corresponding IoU values and subsequently draped over each image at (e) and (f), respectively. The geographical extent of TT1 is roughly 12.3 km by 10.3 km and that of TT10 is roughly 11.3 km by 10.7 km.
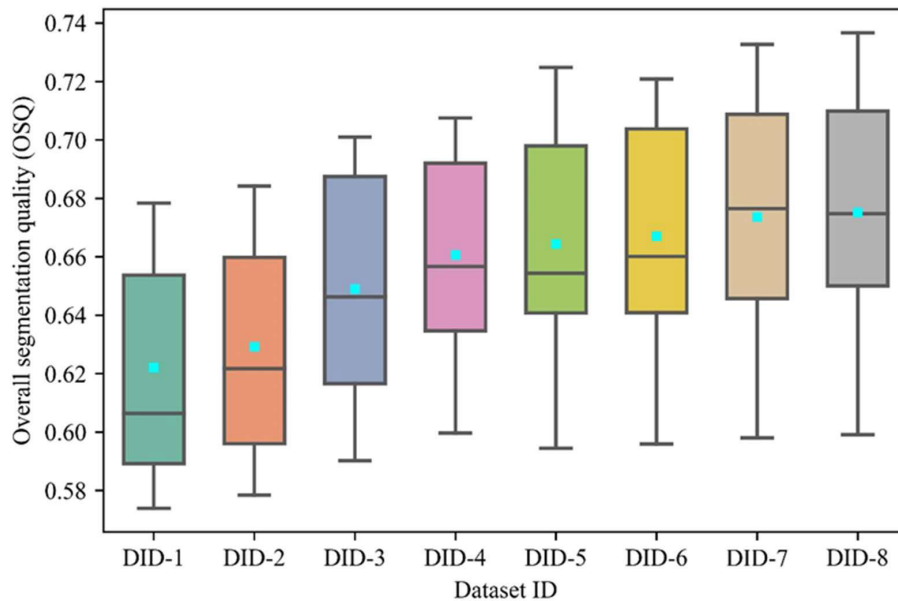
FIGURE 7. Boxplots showing the variability of OSQs obtained at the eleven tiles by the S2S1I-based incremental feature datasets. The cyan boxes are the average OSQs over all tiles as obtained by the incremental feature datasets. The within-box horizontal lines are the median OSQs.
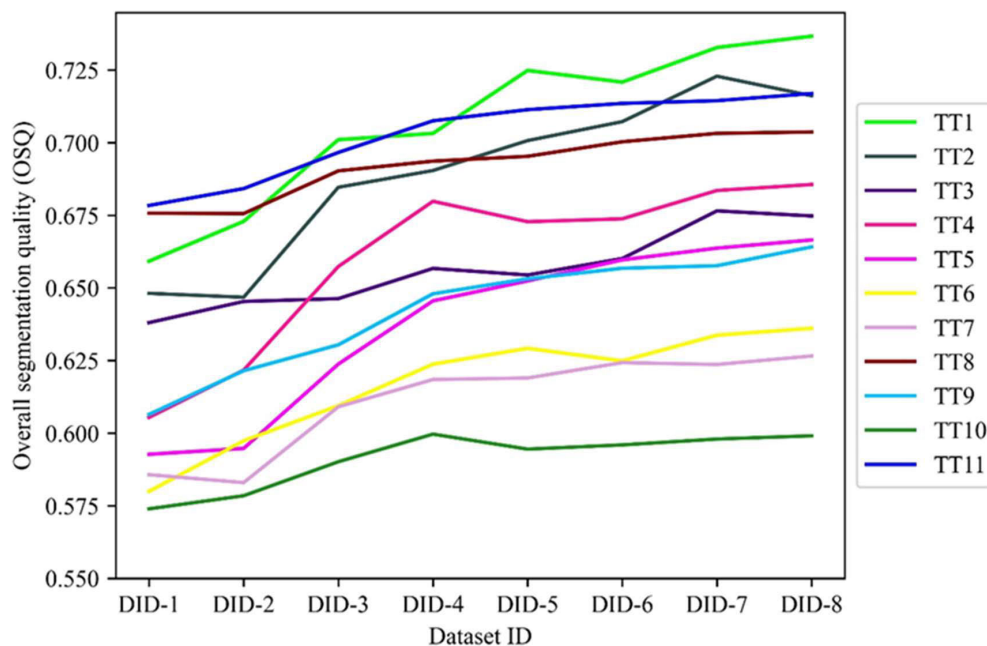
FIGURE 8. The OSQ obtained by each S2S1I-based incremental feature dataset per tile.

remove duplicate segments created due to overlapping tiles and then applied "v.generalize" to simplify the segments. The simplified segments can be viewed as the "simplified_segmentation_ni" layer in this web map.[6] We subsequently applied a majority vote filter to determine the crop type of each segment. As an example, the pixel-based crop type map and the crop type map after the majority vote at TT7 (balanced share of arable lands and grasslands) are captured by Figure 13a and Figure 13b, respectively. The outcome of

the majority vote was a smoothed map, where most of the noise in the pixel-based map had been removed. An accuracy assessment performed using all the GSAA parcels of Lower Saxony indicated an improvement in the overall accuracy after filtering from 78% to 81.4% and the Kappa statistic from 0.705 to 0.747.

V. DISCUSSION

This current study builds on the previous work of [36]. In [36], the authors only focused on the development of the optimization approach. No attention was given to the

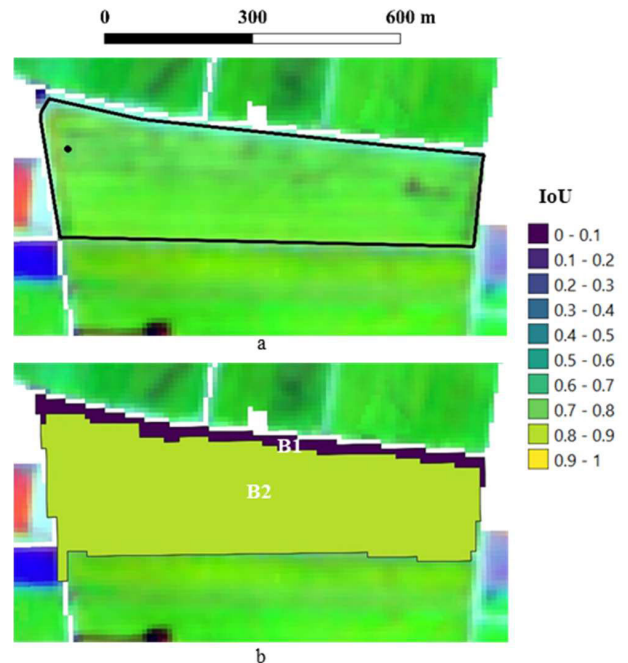[6]https://tisdex.thuenen.de/maps/34/view#/ (Accessed: Jul. 9, 2021).
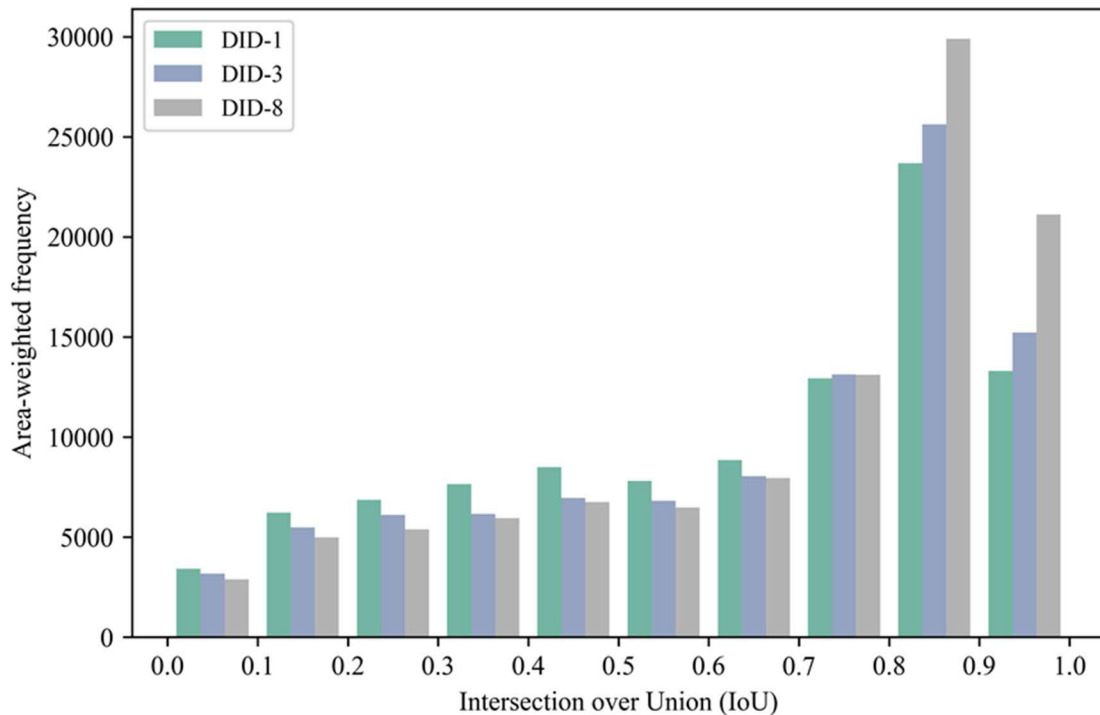
FIGURE 9. Area-weighted histogram of the Intersection over Union (IoU) values computed for the segments in the optimal segmentation results achieved respectively by DID-1, DID-3, and DID-8 at all test tiles.
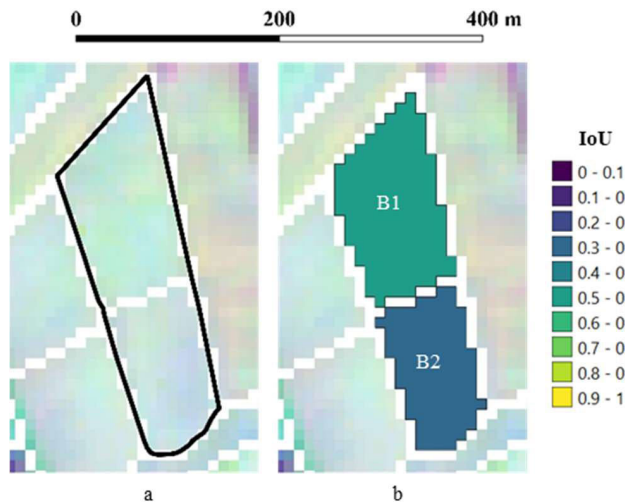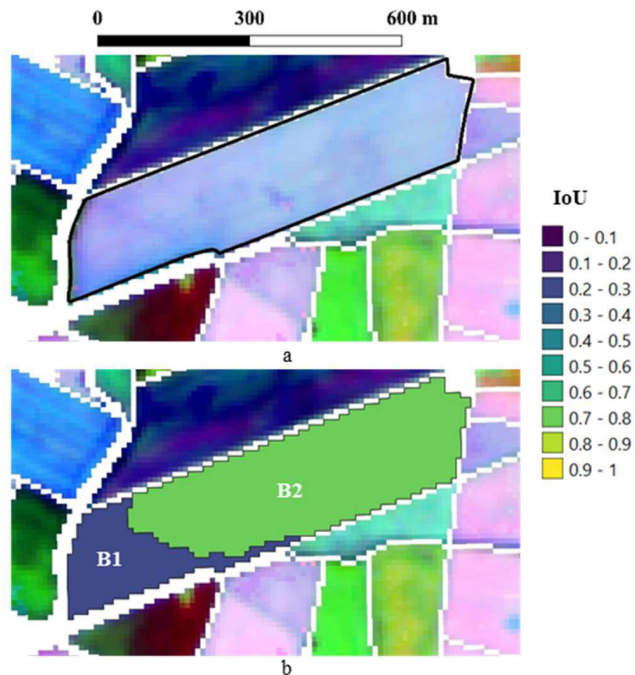

FIGURE 10. Over-segmentation caused by the masking approach used in this study. The background displays in (a) and (b) are based on the false-color image created for DID-8 using the NDVIs of March, June, and October. The image in (a) has been overlaid with the GSAA parcel (black outline). The corresponding segments generated are symbolized in (b) by their IoU values. Two separate segments labeled B1 and B2 were created.

FIGURE 11. Over-segmentation caused by hedges. The background displays in (a) and (b) are based on the false-color image created for DID-8 using the NDVIs of March, June, and October. The image in (a) has been overlaid with the GSAA parcel (black outline). The LU of this GSAA parcel is potato. The corresponding segments generated are symbolized in (b) by their IoU values. Two separate segments labeled B1 and B2 were created.

identification of the optimal feature set for segmenting the agricultural fields. In [36], cloud-free S2 images were manually selected and used. In this study, an automated process based on FORCE was used to identify and replace clouds. This study also evaluated pre-processed S1 datasets as obtained from CODE-DE. For our current study, we used monthly composites of S1 and S2 unlike [36], where single-date S2 images were used. In [36], the segmentation accuracy that could be achieved for different agricultural field size

categories was not assessed. Finally, in this study, the use of image segmentation to aggregate and improve a pixel-based crop type map was evaluated.

FIGURE 12. Over-segmentation caused by the non-optimal MRS parameters. The background displays in (a) and (b) are based on the false-color image created for DID-8 using the NDVIs of March, June, and October. The image in (a) has been overlaid with the GSAA parcel (black outline). The LU of this GSAA parcel is mowing pasture. The corresponding segments generated are symbolized in (b) by their IoU values. Two separate segments labeled B1 and B2 were created.

For segmenting agricultural fields, using only the visible and near-infrared bands (S2B4) of S2 was superior to using all ten bands (S2B10) as depicted in Figure 3. A similar outcome was reported by [23], who received more accurate results using only the visible (RGB) bands of a Worldview-2 image as compared to using all the eight bands for image segmentation based on the MRS algorithm. They attributed this phenomenon to the high correlation existing between the eight bands. To deal with this problem, they applied principal component analysis (PCA) to the eight bands and used the first three components for segmentation. The result was better than using all eight bands but underperformed in comparison with the RGB bands. In using S2, most authors [33]–[40] directly used S2B4 to segment agricultural fields without testing other feature combinations. The superiority of S2B4 to S2B10 as established in this study validates the choice of S2B4 by those authors for segmenting agricultural fields.

Due to the inherently speckled nature of radar images, some researchers [66]–[68] have asserted that the segmentation of optical images is easier and more accurate. Their assertion can largely be backed by Figure 3, where most of the feature sets based on only S2 outperformed those based on only S1. However, the S1 feature sets (S1I, S1BI) containing the radar indices proved capable of segmenting agricultural fields even to the extent that they outperformed S2B10. The speckle noise in radar images often makes it difficult to visually identify the boundaries of features. Monthly compositing was particularly beneficial to S1 as it helped in reducing
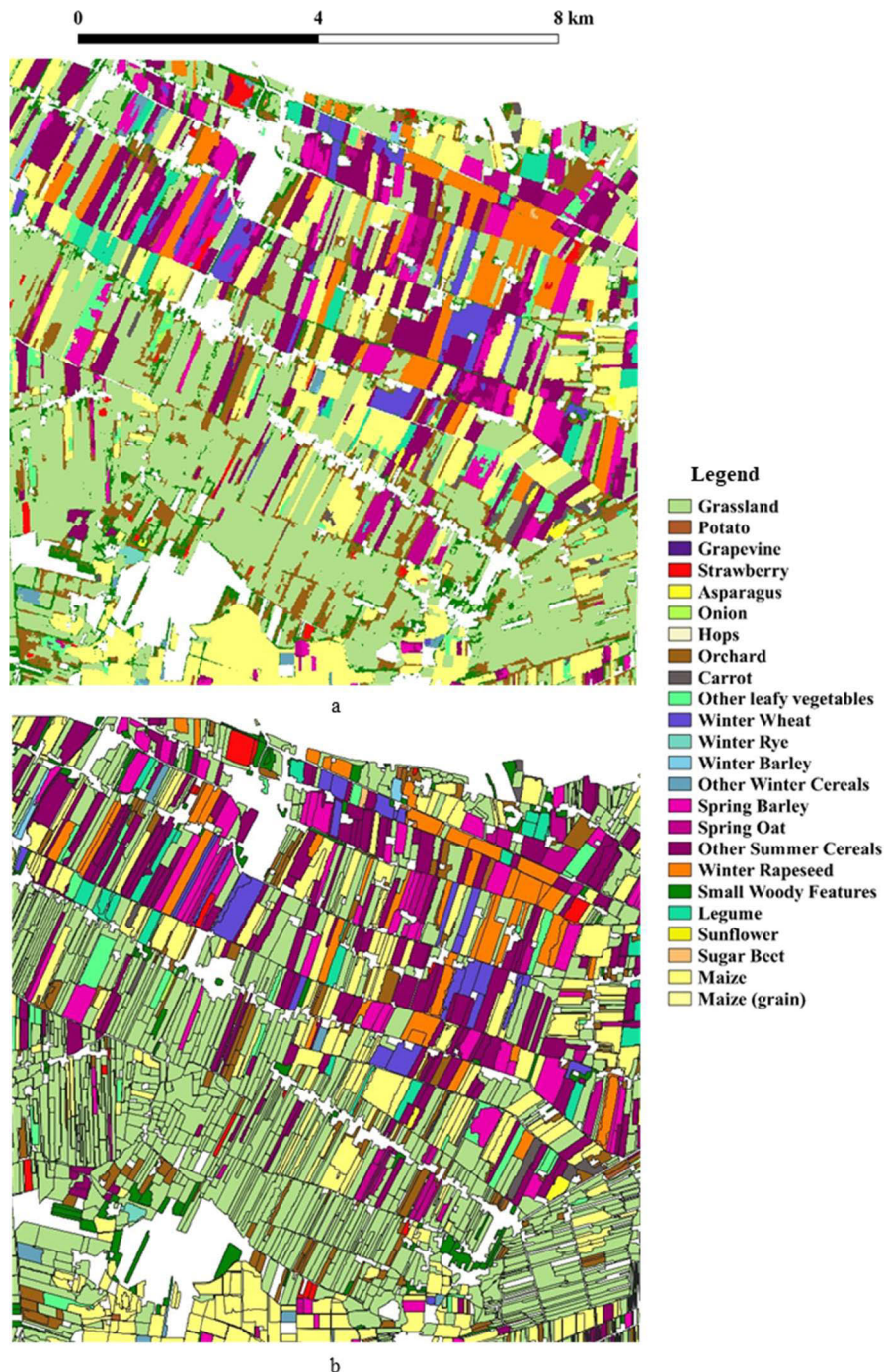
the speckle noise, thereby revealing the boundaries of agricultural fields. The masking approach used in this study was potentially more beneficial to S1 in creating boundaries between adjacent fields. In situations where S2 images are not available due to clouds, monthly composites of S1 images could be used for segmenting agricultural fields. Overall, the combination of S1 and S2 resulted in the highest segmentation accuracy (Figure 3). Within the context of mapping agricultural LU types, other authors [43], [69], [70] also observed that combining S1 and S2 leads to better results than separately using each sensor.

Based on the seasonal feature dataset (DID-8) created from the combined S1 and S2 feature set, the highest OSQ occurred at TT1 (Figure 6e) and the lowest at TT10 (Figure 6f). The main driving forces behind the obtained OSQs were the area and shape of agricultural fields at the tiles. Due to the presence of big and compact agricultural fields at TT1, the segmentation process was more successful there. At TT10, most of the agricultural fields are small and elongated, and additionally, they are highly dominated by one LU (mowing pasture). Such conditions coupled with the spatial resolution of S1 and S2 make it difficult to appropriately segment agricultural fields from S1 and S2 images because clear-cut boundaries between agricultural fields cannot be distinguished in the S1 and S2 images. This observation was also made by [36] in their research as they encountered a similar problem. The use of an image with a higher spatial resolution than S2 was proposed by [36] as a likely solution.

Because agricultural fields are dynamic and change over time, to accurately map different agricultural LU types, the use of multitemporal images is considered a requirement by [71]. With multitemporal images, the different phenological behaviors of different agricultural LU types throughout the growing season can be characterized and effectively used to differentiate them [72]. Although that suggestion was made within the context of image classification, it also applies to the segmentation of agricultural fields as was highlighted by these authors [39], [73]. As Figure 7 shows, using a single-period dataset (DID-1) resulted in segments with significantly lower accuracies than those created using the dataset covering the whole growing season (DID-8). This demonstrates the importance of using multitemporal images for the effective segmentation of agricultural fields. Consecutively increasing the number of images (S2S1I in our case) led to a corresponding increase in the segmentation accuracy (Figure 7). Although these studies [74], [75] were exclusively focused on object classification, they also observed a similar phenomenon, in that, increasing the number of input images yielded an increase in the accuracy of the classified segments.

Some sources of error identified in this study included the masking approach, which led to the over-segmentation captured in Figure 10. This problem could be resolved by using an improved agricultural LC dataset. Another source of error was the presence of hedges in the images, which led to low segmentation accuracies as was highlighted in Figure 11.

Legend
- Grassland
- Potato
- Grapevine
- Strawberry
- Asparagus
- Onion
- Hops
- Orchard
- Carrot
- Other leafy vegetables
- Winter Wheat
- Winter Rye
- Winter Barley
- Other Winter Cereals
- Spring Barley
- Spring Oat
- Other Summer Cereals
- Winter Rapeseed
- Small Woody Features
- Legume
- Sunflower
- Sugar Beet
- Maize
- Maize (grain)

FIGURE 13. Usage of a majority vote to generate an object-based crop type map (b) from the pixel-based crop type map (a).

Although the presence of the hedge led to a low segmentation accuracy, such segmentation errors are acceptable especially for subsequent processes like crop type mapping meant to determine the actual LU within a field. The last source of error as highlighted in Figure 12 was caused by the non-optimal MRS parameters. The segmentation optimization in this study was applied to roughly 11 km by 11 km tiles. In tiles with predominantly smaller fields, such instances of over-segmentation as displayed in Figure 12 are unavoidable.

One solution will be to apply the segmentation optimization based on each GSAA parcel instead of using all parcels within a tile for the optimization. However, such an approach will be computationally expensive. A more efficient solution will be to merge neighboring segments with the same LU type after object classification as was proposed by [36]. After applying the majority vote filter, both segments in Figure 12b were classified as grasslands, hence they could be merged as one segment.
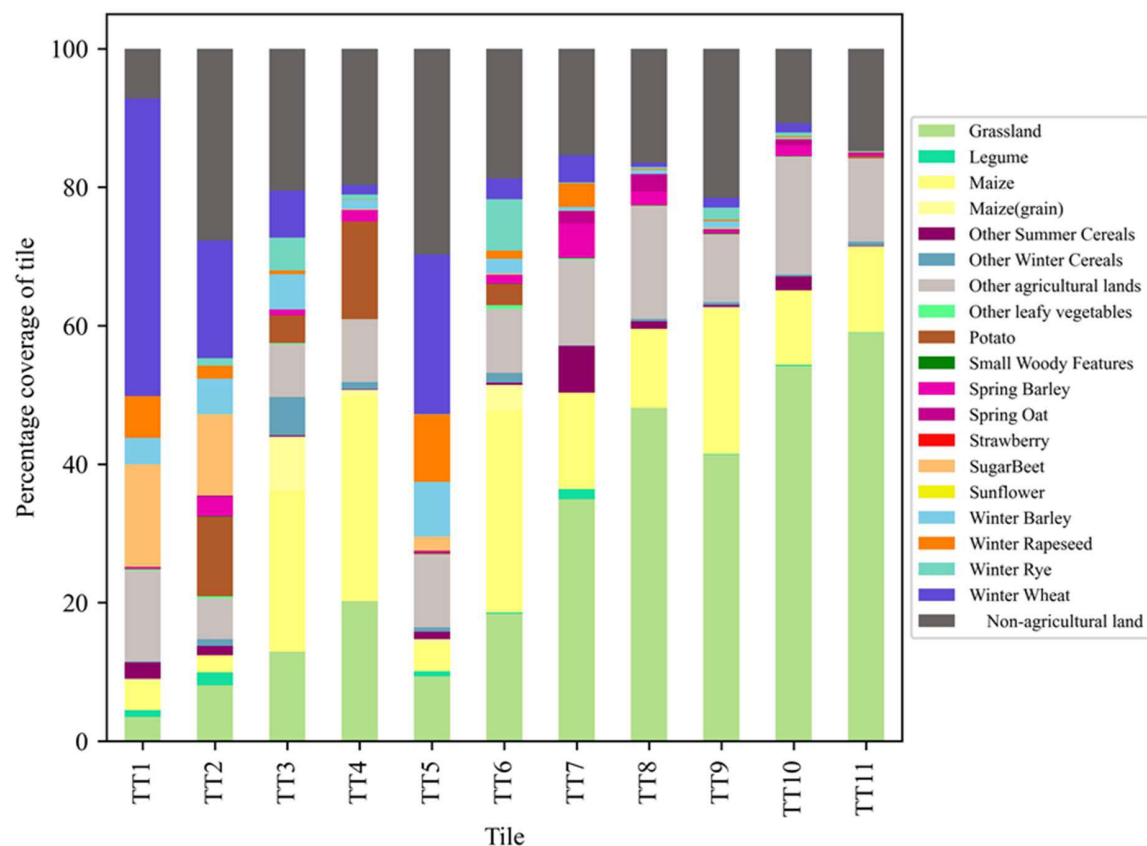
FIGURE 14. Distribution of land-use (LU) per tile.
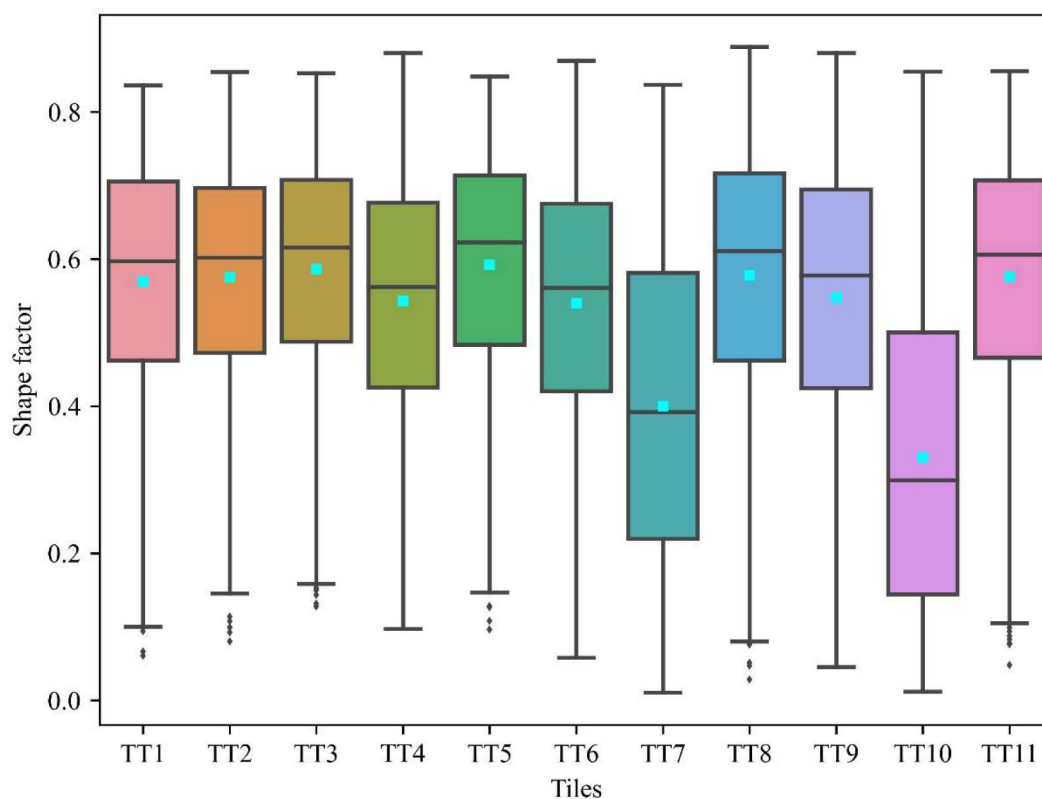
FIGURE 15. The boxplots showing the distribution of shape factors (SFs) per tile. The cyan boxes represent the average SFs. The within-box horizontal lines are the median SFs.

TABLE 5. Basic descriptive information of the GSAA parcels used in this study per test tile.

Tile	No. of GSAA parcels	Min. area (ha)	Max. area (ha)	Mean area (ha)
TT1	1,686	0.21	62.76	5.86
TT2	1,622	0.17	47.78	4.68
TT3	2,694	0.18	23.34	2.97
TT4	2,531	0.20	23.53	3.08
TT5	2,910	0.18	21.85	2.16
TT6	2,354	0.16	29.72	3.48
TT7	1,876	0.19	47.52	3.90
TT8	3,767	0.17	20.74	1.85
TT9	2,015	0.16	49.47	3.76
TT10	2,563	0.20	37.76	2.72
TT11	3,074	0.18	29.47	2.71

TABLE 6. The average OSQs obtained by each feature set over the eleven test tiles.

Feature set	Average OSQ
S1B	0.646
S1BI	0.663
S1I	0.662
S2B10	0.659
S2B10I	0.671
S2B4	0.669
S2B4I	0.671
S2I	0.670
S2S1I	0.675

The general trend discernable from Table 4 is that bigger fields lead to higher segmentation accuracies as was also established in [36]. Contrary to the suggestion of [2] that S1 and S2 are more suitable for large fields, Table 4 rather showed that the S1 and S2 images are more suitable for medium fields. The larger the fields, the higher the probability of over-segmentation as was depicted in Figure 11 and Figure 12, both of which led to lower segmentation accuracies.

The usefulness of image segmentation for post-filtering pixel-based crop type maps was briefly demonstrated in this study. The derived object-based map was more visually appealing and also increased the classification accuracy.

VI. CONCLUSION
In this study, we applied supervised segmentation optimization to different feature datasets generated from S1 and S2 images at eleven test tiles in Lower Saxony, Germany to identify the optimal feature set for segmenting agricultural fields. Additionally, the accuracy of agricultural fields segmented from the S1 and S2 feature datasets between March and October of 2018 was analyzed. Based on the

TABLE 7. The optimal parameter combinations obtained by S1BI (optimal among the S1 feature sets), S2B10I (optimal among the S2 feature sets), and S2S1I (overall optimal feature set) per tile.

Tile	Scale	Shape	Compactness	OSQ	Feature set
TT1	100	0.900	0.865	0.761	S1BI
TT1	80	0.900	0.900	0.724	S2B10I
TT1	97	0.900	0.945	0.737	S2S1I
TT2	108	0.900	1.000	0.685	S1BI
TT2	74	0.900	0.992	0.720	S2B10I
TT2	99	0.899	0.971	0.716	S2S1I
TT3	80	0.900	0.900	0.664	S1BI
TT3	97	0.734	0.757	0.665	S2B10I
TT3	80	0.900	0.700	0.675	S2S1I
TT4	93	0.900	0.918	0.644	S1BI
TT4	95	0.746	0.900	0.680	S2B10I
TT4	80	0.900	0.900	0.686	S2S1I
TT5	70	0.900	1.000	0.670	S1BI
TT5	49	0.900	0.894	0.663	S2B10I
TT5	58	0.900	1.000	0.662	S2S1I
TT6	90	0.900	1.000	0.622	S1BI
TT6	68	0.896	0.783	0.631	S2B10I
TT6	78	0.900	0.984	0.636	S2S1I
TT7	93	0.900	0.398	0.653	S1BI
TT7	90	0.900	0.381	0.623	S2B10I
TT7	103	0.900	0.933	0.628	S2S1I
TT8	66	0.900	0.813	0.676	S1BI
TT8	90	0.690	1.000	0.705	S2B10I
TT8	93	0.759	1.000	0.704	S2S1I
TT9	81	0.900	1.000	0.648	S1BI
TT9	71	0.900	0.935	0.658	S2B10I
TT9	78	0.900	0.830	0.664	S2S1I
TT10	80	0.900	0.500	0.586	S1BI
TT10	135	0.590	0.817	0.593	S2B10I
TT10	132	0.624	0.789	0.599	S2S1I
TT11	80	0.900	0.900	0.687	S1BI
TT11	92	0.810	1.000	0.719	S2B10I
TT11	72	0.900	0.811	0.717	S2S1I

results from the eleven test tiles, the segmentation optimization process was extended to every part of Lower Saxony.

The results obtained in this study allow for the following conclusions to be drawn: (1) S2 generally yields better segmentation results than S1, (2) the synergistic use of S1 and S2 can lead to an improvement in segmentation accuracy, (3) multitemporal S1 and S2 images are key to the optimal segmentation of agricultural fields, (4) S1 and S2 images are more suitable for segmenting medium-sized (1.5 – 15 ha) agricultural fields, and (5) post-filtering of pixel-based crop type maps with agricultural fields extracted via image segmentation improves classification accuracies.

The main outcome (agricultural fields) of this study can be used to produce object-based crop type maps. An object-based crop type map is useful for subsequent processes like the correct estimation of the area per crop type, crop yield modeling, crop rotation analysis, greenhouse gas (GHG) modeling, etc.

Looking ahead, we intend to extend this study to every state in Germany. The derived segmentation results will then be used as direct inputs to land-cover/land-use classification and land-use intensity mapping (mowing detection). To test the robustness of our current approach to the determination of the optimal feature set, we intend to test other segmentation algorithms particularly deep neural networks (DNN), and then compare the results to our current study. Smaller fields are more sensitive to the IoU metric than bigger fields. A small spatial misalignment between a segmented field and its corresponding reference object will have a more negative impact on the IoU value of a smaller field than a bigger field. Therefore, future studies should test other segmentation evaluation metrics that combine the percentages of the overlapped (correctly segmented) area, over-segmented area, and under-segmented area for each segmented field.

APPENDIX A
See Figures 14 and 15, and Tables 5–7.

REFERENCES

[1] United Nations, New York, NY, USA. (Sep. 2015). *Transforming Our World: The 2030 Agenda for Sustainable Development.* Accessed: Jun. 18, 2021. [Online]. Available: https://www.un.org/ga/search/view_doc.asp?symbol=A/RES/70/1&Lang=E

[2] A. K. Whitcraft, I. Becker-Reshef, C. O. Justice, L. Gifford, A. Kavvada, and I. Jarvis, "No pixel left behind: Toward integrating earth observations for agriculture into the united nations sustainable development goals framework," *Remote Sens. Environ.*, vol. 235, Dec. 2019, Art. no. 111470, doi: 10.1016/j.rse.2019.111470.

[3] J. M. Peña-Barragán, M. K. Ngugi, R. E. Plant, and J. Six, "Object-based crop identification using multiple vegetation indices, textural features and crop phenology," *Remote Sens. Environ.*, vol. 115, no. 6, pp. 1301–1316, Jun. 2011, doi: 10.1016/j.rse.2011.01.009.

[4] C. Conrad, S. Fritsch, J. Zeidler, G. Rücker, and S. Dech, "Per-field irrigated crop classification in arid central Asia using SPOT and ASTER data," *Remote Sens.*, vol. 2, no. 4, pp. 1035–1056, Apr. 2010, doi: 10.3390/rs2041035.

[5] J. Meier, W. Mauser, T. Hank, and H. Bach, "Assessments on the impact of high-resolution-sensor pixel sizes for common agricultural policy and smart farming services in European regions," *Comput. Electron. Agricult.*, vol. 169, Feb. 2020, Art. no. 105205, doi: 10.1016/j.compag.2019.105205.

[6] A. García-Pedrero, M. Lillo-Saavedra, D. Rodríguez-Esparragón, and C. Gonzalo-Martín, "Deep learning for automatic outlining agricultural parcels: Exploiting the land parcel identification system," *IEEE Access*, vol. 7, pp. 158223–158236, 2019, doi: 10.1109/ACCESS.2019.2950371.

[7] C. Y. Ji, "Delineating agricultural field boundaries from TM imagery using dyadic wavelet transforms," *ISPRS J. Photogramm. Remote Sens.*, vol. 51, no. 6, pp. 268–283, Dec. 1996, doi: 10.1016/0924-2716(95)00017-8.

[8] C. Atzberger, "Advances in remote sensing of agriculture: Context description, existing operational monitoring systems and major information needs," *Remote Sens.*, vol. 5, no. 2, pp. 949–981, Feb. 2013, doi: 10.3390/rs5020949.

[9] P. Shanmugapriya, S. Rathika, T. Ramesh, and P. Janaki, "Applications of remote sensing in agriculture—A review," *Int. J. Current Microbiol. Appl. Sci.*, vol. 8, no. 1, pp. 2270–2283, Jan. 2019, doi: 10.20546/ijcmas.2019.801.238.

[10] M. Weiss, F. Jacob, and G. Duveiller, "Remote sensing for agricultural applications: A meta-review," *Remote Sens. Environ.*, vol. 236, Jan. 2020, Art. no. 111402, doi: 10.1016/j.rse.2019.111402.

[11] C. Evans, R. Jones, I. Svalbe, and M. Berman, "Segmenting multispectral Landsat TM images into field units," *IEEE Trans. Geosci. Remote Sens.*, vol. 40, no. 5, pp. 1054–1064, May 2002, doi: 10.1109/TGRS.2002.1010893.

[12] M. Möller, L. Lymburner, and M. Volk, "The comparison index: A tool for assessing the accuracy of image segmentation," *Int. J. Appl. Earth Observ. Geoinf.*, vol. 9, no. 3, pp. 311–321, Aug. 2007, doi: 10.1016/j.jag.2006.10.002.

[13] L. Yan and D. P. Roy, "Conterminous United States crop field size quantification from multi-temporal Landsat data," *Remote Sens. Environ.*, vol. 172, pp. 67–86, Jan. 2016, doi: 10.1016/j.rse.2015.10.034.

[14] J. Graesser and N. Ramankutty, "Detection of cropland field parcels from Landsat imagery," *Remote Sens. Environ.*, vol. 201, pp. 165–180, Nov. 2017, doi: 10.1016/j.rse.2017.08.027.

[15] L. Yan and D. P. Roy, "Automated crop field extraction from multi-temporal web enabled Landsat data," *Remote Sens. Environ.*, vol. 144, pp. 42–64, Mar. 2014, doi: 10.1016/j.rse.2014.01.006.

[16] J. A. Long, R. L. Lawrence, M. C. Greenwood, L. Marshall, and P. R. Miller, "Object-oriented crop classification using multitemporal ETM+SLC-off imagery and random forest," *GISci. Remote Sens.*, vol. 50, no. 4, pp. 418–436, Aug. 2013, doi: 10.1080/15481603.2013.817150.

[17] J. K. Gilbertson, J. Kemp, and A. Van Niekerk, "Effect of pan-sharpening multi-temporal Landsat 8 imagery for crop type differentiation using different classification techniques," *Comput. Electron. Agricult.*, vol. 134, pp. 151–159, Mar. 2017, doi: 10.1016/j.compag.2016.12.006.

[18] B. Schultz, M. Immitzer, A. Formaggio, I. Sanches, A. Luiz, and C. Atzberger, "Self-guided segmentation and classification of multi-temporal Landsat 8 images for crop type mapping in Southeastern Brazil," *Remote Sens.*, vol. 7, no. 11, pp. 14482–14508, Oct. 2015, doi: 10.3390/rs71114482.

[19] K. Johansen, O. Lopez, Y.-H. Tu, T. Li, and M. F. McCabe, "Center pivot field delineation and mapping: A satellite-driven object-based image analysis approach for national scale accounting," *ISPRS J. Photogramm. Remote Sens.*, vol. 175, pp. 1–19, May 2021, doi: 10.1016/j.isprsjprs.2021.02.019.

[20] H. Yang, B. Pan, W. Wu, and J. Tai, "Field-based rice classification in Wuhua county through integration of multi-temporal Sentinel-1A and Landsat-8 OLI data," *Int. J. Appl. Earth Observ. Geoinf.*, vol. 69, pp. 226–236, Jul. 2018, doi: 10.1016/j.jag.2018.02.019.

[21] T. Blaschke, "Object based image analysis for remote sensing," *ISPRS J. Photogram. Remote Sens.*, vol. 65, no. 1, pp. 2–16, Jan. 2010, doi: 10.1016/j.isprsjprs.2009.06.004.

[22] T. Blaschke, S. Lang, E. Lorup, J. Strobl, and P. Zeil, "Object-oriented image processing in an integrated GIS/remote sensing environment and perspectives for environmental applications," *Environ. Inf. Planning, Politics Public*, vol. 2, pp. 555–570, Oct. 2000.

[23] N. Mesner and K. Oštir, "Investigating the impact of spatial and spectral resolution of satellite images on segmentation quality," *J. Appl. Remote Sens.*, vol. 8, no. 1, Jan. 2014, Art. no. 083696, doi: 10.1117/1.JRS.8.083696.

[24] European Commission. (2017). *CAP Explained: Direct Payments for Farmers 2015–2020. LU: Publications Office.* Accessed: Mar. 12, 2021. [Online]. Available: https://data.europa.eu/doi/10.2762/572019

[25] G. Forkuor, C. Conrad, M. Thiel, T. Ullmann, and E. Zoungrana, "Integration of optical and synthetic aperture radar imagery for improving crop mapping in northwestern Benin, West Africa," *Remote Sens.*, vol. 6, no. 7, pp. 6472–6499, Jul. 2014, doi: 10.3390/rs6076472.

[26] C. Persello, V. A. Tolpekin, J. R. Bergado, and R. A. de By, "Delineation of agricultural fields in smallholder farms from satellite images using fully convolutional networks and combinatorial grouping," *Remote Sens. Environ.*, vol. 231, Sep. 2019, Art. no. 111253, doi: 10.1016/j.rse.2019.111253.

[27] I. L. Castillejo-González, F. López-Granados, A. García-Ferrer, J. M. Peña-Barragán, M. Jurado-Expósito, M. S. de la Orden, and M. González-Audicana, "Object- and pixel-based analysis for mapping crops and their agro-environmental associated measures using QuickBird imagery," *Comput. Electron. Agricult.*, vol. 68, no. 2, pp. 207–215, Oct. 2009, doi: 10.1016/j.compag.2009.06.004.

[28] P. Defourny *et al.*, "Near real-time agriculture monitoring at national scale at parcel resolution: Performance assessment of the Sen2-Agri automated system in various cropping systems around the world," *Remote Sens. Environ.*, vol. 221, pp. 551–568, Feb. 2019, doi: 10.1016/j.rse.2018.11.007.

[29] C. Luo, B. Qi, H. Liu, D. Guo, L. Lu, Q. Fu, and Y. Shao, "Using time series Sentinel-1 images for object-oriented crop classification in Google earth engine," *Remote Sens.*, vol. 13, no. 4, p. 561, Feb. 2021, doi: 10.3390/rs13040561.

[30] K. Clauss, M. Ottinger, and C. Kuenzer, "Mapping rice areas with Sentinel-1 time series and superpixel segmentation," *Int. J. Remote Sens.*, vol. 39, no. 5, pp. 1399–1420, Mar. 2018, doi: 10.1080/01431161.2017.1404162.

[31] M. P. Wagner and N. Oppelt, "Extracting agricultural fields from remote sensing imagery using graph-based growing contours," *Remote Sens.*, vol. 12, no. 7, p. 1205, Apr. 2020, doi: 10.3390/rs12071205.

[32] A. Nasrallah, N. Baghdadi, M. Mhawej, G. Faour, T. Darwish, H. Belhouchette, and S. Darwich, "A novel approach for mapping wheat areas using high resolution Sentinel-2 images," *Sensors*, vol. 18, no. 7, p. 2089, Jun. 2018, doi: 10.3390/s18072089.

[33] O. Csillik, M. Belgiu, G. P. Asner, and M. Kelly, "Object-based time-constrained dynamic time warping classification of crops using Sentinel-2," *Remote Sens.*, vol. 11, no. 10, p. 1257, May 2019, doi: 10.3390/rs11101257.

[34] B. Watkins and A. Van Niekerk, "Automating field boundary delineation with multi-temporal Sentinel-2 imagery," *Comput. Electron. Agricult.*, vol. 167, Dec. 2019, Art. no. 105078, doi: 10.1016/j.compag.2019.105078.

[35] F. Waldner and F. I. Diakogiannis, "Deep learning on edge: Extracting field boundaries from satellite images with a convolutional neural network," *Remote Sens. Environ.*, vol. 245, Aug. 2020, Art. no. 111741, doi: 10.1016/j.rse.2020.111741.

[36] G. O. Tetteh, A. Gocht, and C. Conrad, "Optimal parameters for delineating agricultural parcels from satellite images based on supervised Bayesian optimization," *Comput. Electron. Agricult.*, vol. 178, Nov. 2020, Art. no. 105696, doi: 10.1016/j.compag.2020.105696.

[37] G. O. Tetteh, A. Gocht, M. Schwieder, S. Erasmi, and C. Conrad, "Unsupervised parameterization for optimal segmentation of agricultural parcels from satellite images in different agricultural landscapes," *Remote Sens.*, vol. 12, no. 18, p. 3096, Sep. 2020, doi: 10.3390/rs12183096.

[38] M. Vogels, S. de Jong, G. Sterk, H. Douma, and E. Addink, "Spatio-temporal patterns of smallholder irrigated agriculture in the horn of Africa using GEOBIA and Sentinel-2 imagery," *Remote Sens.*, vol. 11, no. 2, p. 143, Jan. 2019, doi: 10.3390/rs11020143.

[39] B. Watkins and A. van Niekerk, "A comparison of object-based image analysis approaches for field boundary delineation using multi-temporal Sentinel-2 imagery," *Comput. Electron. Agricult.*, vol. 158, pp. 294–302, Mar. 2019, doi: 10.1016/j.compag.2019.02.009.

[40] M. Belgiu and O. Csillik, "Sentinel-2 cropland mapping using pixel-based and object-based time-weighted dynamic time warping analysis," *Remote Sens. Environ.*, vol. 204, pp. 509–523, Jan. 2018, doi: 10.1016/j.rse.2017.10.005.

[41] M. Baatz and A. Schäpe, "Multiresolution segmentation: An optimization approach for high quality multi-scale image segmentation," in *Angewandte Geographische Informations-Verarbeitung XII*, J. Strobl, T. Blaschke, and G. Griesebner, Eds. Karlsruhe, Germany: Wichmann Verlag, 2000, pp. 12–23.

[42] *eCognition Developer 9.5.0 Reference Book*, Trimble Germany GmbH, Munich, Germany, 2019.

[43] C. Luo, H.-J. Liu, L.-P. Lu, Z.-R. Liu, F.-C. Kong, and X.-L. Zhang, "Monthly composites from Sentinel-1 and Sentinel-2 images for regional major crop mapping with Google earth engine," *J. Integrative Agricult.*, vol. 19, pp. 2–15, Jul. 2020.

[44] U. Benz, I. Banovsky, A. Cesarz, and M. Schmidt. (2020). *CODE-DE Portal Handbook, Version 2.0. Germany: DLR.* Accessed: Mar. 23, 2021. [Online]. Available: https://code-de.cdn.prismic.io/code-de/ff151913-16e0-4dc3-8005-696bf25bf65d_User+Manual_v2.0.2_ENG.pdf

[45] D. Frantz, "FORCE—Landsat + Sentinel-2 analysis ready data and beyond," *Remote Sens.*, vol. 11, no. 9, p. 1124, May 2019, doi: 10.3390/rs11091124.

[46] J. Buchner, H. Yin, D. Frantz, T. Kuemmerle, E. Askerov, T. Bakuradze, B. Bleyhl, N. Elizbarashvili, A. Komarova, K. E. Lewińska, A. Rizayeva, H. Sayadyan, B. Tan, G. Tepanosyan, N. Zazanashvili, and V. C. Radeloff, "Land-cover change in the caucasus mountains since 1987 based on the topographic correction of multi-temporal Landsat composites," *Remote Sens. Environ.*, vol. 248, Oct. 2020, Art. no. 111967, doi: 10.1016/j.rse.2020.111967.

[47] D. Frantz, A. Roder, M. Stellmes, and J. Hill, "An operational radiometric Landsat preprocessing framework for large-area time series applications," *IEEE Trans. Geosci. Remote Sens.*, vol. 54, no. 7, pp. 3928–3943, Jul. 2016, doi: 10.1109/TGRS.2016.2530856.

[48] D. Roy, Z. Li, and H. Zhang, "Adjustment of Sentinel-2 multi-spectral instrument (MSI) red-edge band reflectance to nadir BRDF adjusted reflectance (NBAR) and quantification of red-edge band BRDF effects," *Remote Sens.*, vol. 9, no. 12, p. 1325, Dec. 2017, doi: 10.3390/rs9121325.

[49] D. Frantz, E. Haß, A. Uhl, J. Stoffels, and J. Hill, "Improvement of the Fmask algorithm for Sentinel-2 images: Separating clouds from bright surfaces based on parallax effects," *Remote Sens. Environ.*, vol. 215, pp. 471–481, Sep. 2018, doi: 10.1016/j.rse.2018.04.046.

[50] Z. Zhu, S. Wang, and C. E. Woodcock, "Improvement and expansion of the Fmask algorithm: Cloud, cloud shadow, and snow detection for Landsats 4–7, 8, and Sentinel 2 images," *Remote Sens. Environ.*, vol. 159, pp. 269–277, Mar. 2015, doi: 10.1016/j.rse.2014.12.014.

[51] Z. Zhu and C. E. Woodcock, "Object-based cloud and cloud shadow detection in Landsat imagery," *Remote Sens. Environ.*, vol. 118, pp. 83–94, Mar. 2012, doi: 10.1016/j.rse.2011.10.028.

[52] M. Schwieder, P. J. Leitão, M. M. da Cunha Bustamante, L. G. Ferreira, A. Rabe, and P. Hostert, "Mapping Brazilian savanna vegetation gradients with Landsat time series," *Int. J. Appl. Earth Observ. Geoinf.*, vol. 52, pp. 361–370, Oct. 2016, doi: 10.1016/j.jag.2016.06.019.

[53] A. Novelli, M. Aguilar, F. Aguilar, A. Nemmaoui, and E. Tarantino, "AssesSeg—A command line tool to quantify image segmentation quality: A test carried out in southern Spain from satellite imagery," *Remote Sens.*, vol. 9, no. 1, p. 40, Jan. 2017, doi: 10.3390/rs9010040.

[54] D. D. Polsby and R. Popper, "The third criterion: Compactness as a procedural safeguard against partisan gerrymandering," Social Sci. Res. Netw., Rochester, NY, USA, Tech. Rep. 2936284, Mar. 1991, doi: 10.2139/ssrn.2936284.

[55] X. Blaes, P. Defourny, U. Wegmuller, A. D. Vecchia, L. Guerriero, and P. Ferrazzoli, "C-band polarimetric indexes for maize monitoring based on a validated radiative transfer model," *IEEE Trans. Geosci. Remote Sens.*, vol. 44, no. 4, pp. 791–800, Apr. 2006, doi: 10.1109/TGRS.2005.860969.

[56] R. Nasirzadehdizaji, F. B. Sanli, S. Abdikan, Z. Cakir, A. Sekertekin, and M. Ustuner, "Sensitivity analysis of multi-temporal Sentinel-1 SAR parameters to crop height and canopy coverage," *Appl. Sci.*, vol. 9, no. 4, p. 655, Feb. 2019, doi: 10.3390/app9040655.

[57] A. A. Gitelson, Y. J. Kaufman, R. Stark, and D. Rundquist, "Novel algorithms for remote estimation of vegetation fraction," *Remote Sens. Environ.*, vol. 80, pp. 76–87, Apr. 2002, doi: 10.1016/S0034-4257(01)00289-9.

[58] W. Rouse and R. H. Haas, "Monitoring vegetation systems in the great plains with ERTS," in *Proc. Earth Resour. Technol. Satell. Symp.*, Washington, DC, USA, vol. 1, 1973, pp. 309–317.

[59] J. Qi, R. Marsett, R. Heilman, S. Bieden-Bender, S. Moran, D. Goodrich, and M. Weltz, "RANGES improves satellite-based information and land cover assessments in southwest United States," *Eos Trans. Amer. Geophys. Union*, vol. 83, no. 51, pp. 601–606, 2002, doi: 10.1029/2002EO000411.

[60] E. M. Barnes, T. R. Clarke, S. E. Richards, P. D. Colaizzi, J. Haberland, M. Kostrzewski, P. Waller, C. Choi, E. Riley, T. Thompson, R. J. Lascano, H. Li, and M. S. Moran, "Coincident detection of crop water stress, nitrogen status and canopy density using ground based multispectral data," in *Proc. 5th Int. Conf. Precis. Agricult.*, Bloomington, MN, USA, vol. 1619, 2000, p. 15.

[61] B.-C. Gao, "NDWI—A normalized difference water index for remote sensing of vegetation liquid water from space," *Remote Sens. Environ.*, vol. 58, no. 3, pp. 257–266, Dec. 1996, doi: 10.1016/S0034-4257(96)00067-3.

[62] A. P. van Deventer, A. D. Ward, P. H. Gowda, and J. G. Lyon, "Using thematic mapper data to identify contrasting soil plains and tillage practices," *Photogramm. Eng. Remote Sens.*, vol. 63, no. 1, pp. 87–93, 1997.

[63] P. Jaccard, "Etude de la distribution florale dans une portion des Alpes et du Jura," *Bull. de la Societe Vaudoise des Sciences Naturelles* vol. 37, pp. 547–579, Jan. 1901, doi: 10.5169/seals-266450.

[64] S. Valero, D. Morin, J. Inglada, G. Sepulcre, M. Arias, O. Hagolle, G. Dedieu, S. Bontemps, P. Defourny, and B. Koetz, "Production of a dynamic cropland mask by processing remote sensing image series at high temporal and spatial resolutions," *Remote Sens.*, vol. 8, no. 1, p. 55, Jan. 2016, doi: 10.3390/rs8010055.

[65] L. Blickensdörfer, M. Schwieder, D. Pflugmacher, S. Erasmi, C. Nendel, and P. Hostert, "Multi-year national-scale crop type mapping with combined time series of Sentinel-1, Sentinel-2 and Landsat 8 data," *Remote Sens. Environ.*, to be published.

[66] Y. Cai, X. Li, M. Zhang, and H. Lin, "Mapping wetland using the object-based stacked generalization method based on multi-temporal optical and SAR data," *Int. J. Appl. Earth Observ. Geoinf.*, vol. 92, Oct. 2020, Art. no. 102164, doi: 10.1016/j.jag.2020.102164.

[67] S. Mahdavi, B. Salehi, M. Amani, J. E. Granger, B. Brisco, W. Huang, and A. Hanson, "Object-based classification of wetlands in New-foundland and Labrador using multi-temporal PolSAR data," *Can. J. Remote Sens.*, vol. 43, no. 5, pp. 432–450, Sep. 2017, doi: 10.1080/07038992.2017.1342206.

[68] G. Shuai, J. Zhang, B. Basso, Y. Pan, X. Zhu, S. Zhu, and H. Liu, "Multi-temporal RADARSAT-2 polarimetric SAR for maize mapping supported by segmentations from high-resolution optical image," *Int. J. Appl. Earth Observ. Geoinf.*, vol. 74, pp. 1–15, Feb. 2019, doi: 10.1016/j.jag.2018.08.021.

[69] M. Campos-Taberner, F. J. García-Haro, B. Martínez, S. Sánchez-Ruiz, and M. A. Gilabert, "A Copernicus Sentinel-1 and Sentinel-2 classification framework for the 2020+European common agricultural policy: A case study in València (Spain)," *Agronomy*, vol. 9, no. 9, p. 556, Sep. 2019, doi: 10.3390/agronomy9090556.

[70] K. Van Tricht, A. Gobin, S. Gilliams, and I. Piccard, "Synergistic use of radar Sentinel-1 and optical Sentinel-2 imagery for crop mapping: A case study for Belgium," *Remote Sens.*, vol. 10, no. 10, p. 1642, Oct. 2018, doi: 10.3390/rs10101642.

[71] G. Waldhoff, C. Curdt, D. Hoffmeister, and G. Bareth, "Analysis of multi-temporal and multisensor remote sensing data for crop rotation mapping," *ISPRS Ann. Photogramm., Remote Sens. Spatial Inf. Sci.*, vol. 1, no. 7, pp. 177–182, Jul. 2012.

[72] J. Inglada, J.-F. Dejoux, O. Hagolle, and G. Dedieu, "Multi-temporal remote sensing image segmentation of croplands constrained by a topographical database," in *Proc. IEEE Int. Geosci. Remote Sens. Symp.*, Munich, Germany, Jul. 2012, pp. 6781–6784, doi: 10.1109/IGARSS.2012.6352607.

[73] H. C. North, D. Pairman, and S. E. Belliss, "Boundary delineation of agricultural fields in multitemporal satellite imagery," *IEEE J. Sel. Topics Appl. Earth Observ. Remote Sens.*, vol. 12, no. 1, pp. 237–251, Jan. 2019, doi: 10.1109/JSTARS.2018.2884513.

[74] C. Conrad, S. Dech, O. Dubovyk, S. Fritsch, D. Klein, F. Löw, G. Schorcht, and J. Zeidler, "Derivation of temporal windows for accurate crop discrimination in heterogeneous croplands of uzbekistan using multitemporal RapidEye images," *Comput. Electron. Agricult.*, vol. 103, pp. 63–74, Apr. 2014, doi: 10.1016/j.compag.2014.02.003.

[75] Q. Song, Q. Hu, Q. Zhou, C. Hovis, M. Xiang, H. Tang, and W. Wu, "In-season crop mapping with GF-1/WFV data by combining object-based image analysis and random forest," *Remote Sens.*, vol. 9, no. 11, p. 1184, Nov. 2017, doi: 10.3390/rs9111184.

GIDEON OKPOTI TETTEH was born in Accra, Ghana. He received the M.Sc. degree in photogrammetry and geoinformatics from Stuttgart University of Applied Sciences, in 2012. He is currently pursuing the Ph.D. degree with Martin-Luther-University Halle-Wittenberg, Halle (Saale), Germany.

From October 2012 to July 2017, he worked as a Remote Sensing Application Developer with Planet Labs Germany GmbH, Berlin. Since August 2017, he has been working as a Scientific Researcher with Thünen Institute of Farm Economics, Braunschweig.

ALEXANDER GOCHT received the degree in agricultural studies from the Imperial College of London, and the Ph.D. degree from the University of Bonn, Germany, in 2009, with a focus on methods of economic farm modeling.

Since 2004, he has been a Senior Research Fellow with Thünen Institute of Farm Economics, Braunschweig, and works in close cooperation with the CAPRI Modeling Group. He is one of the CAPRI Core Developers. From 2017 to 2020, he coordinated the working group for remote sensing (RS) at Thünen Institute and since then, he has been closely involved in the methodological development of remote sensing applications for modeling purposes. He has contributed to various studies to the development models aiming to assess the impacts of the Common Agricultural Policy (CAP) on farm economics and environmental effects. He has also undertaken various quantitative analyses of agricultural and environmental policies. He continuously researches farm typology particularly on developing methods for consistent aggregation.

STEFAN ERASMI was born in Bremen, Germany, in 1969. He received the Diploma and Ph.D. degrees in geography from the University of Göttingen, in 1997 and 2002, respectively.

From 2002 to 2019, he worked in research and education at the Institute of Geography, University of Göttingen. Since 2019, he has been a Senior Research Scientist with Thünen Institute of Farm Economics, Braunschweig. He has long experience in monitoring agricultural land-use and land-cover, agricultural practices, landscape patterns, and forest parameters from multi-source satellite data for applications in ecology and socio-economics. At Thünen Institute, he is leading the Thünen Earth Observation (ThEO) Working Group that provides EO-based area-wide solutions and objective information for policymakers in terms of the impact assessment of political decisions as well as societal and environmental trends. He is an Editor of the *Journal of Photogrammetry, Remote Sensing and Geoinformation Science* (PFG).

MARCEL SCHWIEDER received the M.Sc. degree in physical geography and the Ph.D. degree with a focus on the phenological analysis of Cerrado vegetation using Landsat time series from Humboldt University, Berlin, in 2013 and 2018, respectively.

From 2013 to 2017, he was a Research Assistant with the Geomatics Laboratory, Humboldt University. From 2018 to 2021, he was a Postdoctoral Researcher with the Geomatics Laboratory, Humboldt University. Since March 2021, he has been working as a Scientific Researcher with Thünen Institute of Farm Economics, Braunschweig. He is also a Guest Scientist with the Earth Observation Laboratory, Humboldt University.

CHRISTOPHER CONRAD was born in Alzenau, Germany, in 1974. He received the Diploma degree in geography from the University of Mainz, Germany, in 2002, and the Ph.D. degree in geography from the University of Würzburg, Germany, in 2006.

From 2006 to 2011, he was a Research Assistant and a Lecturer in the framework of the Bavarian Elite Network at the Universities of Bayreuth and Würzburg, Germany. From 2011 to 2017, he was a Junior Professor of geographical remote sensing with the University of Würzburg. Since 2017, he has been representing the professorship of geoecology with the University of Halle-Wittenberg, Germany, as a Substitute Professor, and took over the full professorship, in 2019. He is an author of over 70 peer-reviewed articles in the field of remote sensing for sustainable land and water management, in particular of agricultural landscapes, with a regional focus on Central Asia and Central Europe. He is an Editor of the *Journal of Photogrammetry, Remote Sensing, and Geoinformation Science* (PFG).

. . .